

1  
2  
3  
4  
5  
6  
7  
8  
9  
10  
11  
12  
13  
14  
15  
16  
17  
18  
19  
20  
21  
22  
23  
24  
25  
26  
27  
28  
29

***Mtfp1* ablation enhances mitochondrial respiration and protects against hepatic steatosis**

Cecilia PATITUCCI<sup>1\*</sup>, Juan Diego HERNÁNDEZ-CAMACHO<sup>1\*</sup>, Elodie VIMONT<sup>1</sup>, Thomas COKELAER<sup>2,3</sup>, Thibault CHAZE<sup>4</sup>, Quentin GIAI GIANETTO<sup>3,4</sup>, Mariette MATONDO<sup>3</sup>, Anastasia GAZI<sup>5</sup>, Ivan NEMAZANY<sup>6</sup>, David A. STROUD<sup>7</sup>, Daniella H. HOCK<sup>7</sup>, Erminia DONNARUMMA<sup>1</sup>, Timothy WAI<sup>1\*\*</sup>

*1- Institut Pasteur, Mitochondrial Biology Group, CNRS UMR 3691, Université Paris Cité, Paris, France.*

*2- Institut Pasteur, Biomix Technological Platform, Université Paris Cité, Paris, France*

*3- Institut Pasteur, Bioinformatics and Biostatistics Hub, Université Paris Cité, Paris, France*

*4- Institut Pasteur, Proteomics Core Facility, MSBio UtechS, UAR CNRS 2024, Université Paris Cité, Paris, France*

*5- Institut Pasteur Ultrastructural Bio Imaging, UTechS, Université Paris Cité, Paris, France.*

*6- Platform for Metabolic Analyses, SFR Necker, INSERM US24/CNRS UAR 3633, Paris, France.*

*7- Department of Biochemistry and Pharmacology, Bio21 Molecular Science and Biotechnology Institute, University of Melbourne, Victorian Clinical Genetics Services and Murdoch Children's Research Institute, Royal Children's Hospital, Melbourne, Australia*

\*These authors contributed equally to this work

\*\*Correspondence: [timothy.wai@pasteur.fr](mailto:timothy.wai@pasteur.fr)

Keywords : **mitochondria, liver, steatosis, NAFLD, oxidative phosphorylation**

30 **Abstract**

31 Hepatic steatosis is the result of an imbalance between nutrient delivery and metabolism in the  
32 liver. It is the first hallmark of Non-alcoholic fatty liver disease (NAFLD) and is characterized by the  
33 accumulation of excess lipids in the liver that can drive liver failure, inflammation, and cancer.  
34 Mitochondria control the fate and function of cells and compelling evidence implicates these  
35 multifunctional organelles in the appearance and progression of liver dysfunction, although it  
36 remains to be elucidated which specific mitochondrial functions are actually causally linked to  
37 NAFLD. Here, we identified Mitochondrial Fission Process 1 protein (MTFP1) as a key regulator of  
38 mitochondrial and metabolic activity in the liver. Deletion of *Mtfp1* in hepatocytes is physiologically  
39 benign in mice yet leads to the upregulation of oxidative phosphorylation (OXPHOS) activity and  
40 mitochondrial respiration, independently of mitochondrial biogenesis. Consequently, hepatocyte-  
41 specific knockout mice are protected against high fat diet-induced hepatic steatosis and metabolic  
42 dysregulation. Additionally, we find that deletion of *Mtfp1* in liver mitochondria inhibits  
43 mitochondrial permeability transition pore opening in hepatocytes, conferring protection against  
44 apoptotic liver damage in vivo and ex vivo. Our work uncovers novel functions of MTFP1 in the  
45 liver, positioning this gene as an unexpected regulator of OXPHOS and a therapeutic candidate for  
46 NAFLD.

## 47 **Introduction**

48 Non-alcoholic fatty liver disease (NAFLD) is the most common chronic liver disease in  
49 industrialized countries, whose incidence is rapidly expanding worldwide<sup>1</sup>. NAFLD is a frequent  
50 comorbidity of type 2 diabetes and obesity with its prevalence calculated at ~30% in the general  
51 population and 80% among obese people. NAFLD encompasses a spectrum of pathologies  
52 ranging from simple steatosis characterized by triglyceride accumulation in hepatocytes, to non-  
53 alcoholic steatohepatitis (NASH), whose hallmarks are inflammation and fibrogenesis, which can  
54 further progress into cirrhosis and hepato-cellular carcinoma (HCC), the deadliest form of liver  
55 cancer<sup>2</sup>.

56 Considerable efforts have been made in recent decades to better understand the  
57 mechanisms of NAFLD progression and therapeutic targets that might subsequently alleviate the  
58 burden of this spectrum of pathologies. The progression of NAFLD is currently explained by a  
59 “multiple parallel-hit” hypothesis, which implicates the synergistic and concerted action of multiple  
60 events originating from various liver cell types<sup>3</sup>. In hepatocytes, oxidative stress and mitochondrial  
61 dysfunction have been suggested to contribute to hepatocyte damage and death, tissue  
62 inflammation and fibrosis<sup>4</sup>. This model highlights the complexity and heterogeneity of NAFLD  
63 progression and underscores the central involvement of hepatocytes mitochondria in the  
64 progression of NAFLD. Mitochondria are essential organelles that are deeply integrated in cellular  
65 homeostasis. Most famous for their production of ATP via oxidative phosphorylation (OXPHOS),  
66 mitochondria also regulate programmed cell death and inflammation through the sequestration and  
67 release of pro-apoptotic factors and pro-inflammatory molecules<sup>5,6</sup>. Yet which of the multiple  
68 functions of mitochondria are directly implicated in the onset of steatosis, inflammation, hepatocyte  
69 death, and subsequent tissue remodeling has not been defined<sup>7</sup>.

70 The relevance of mitochondria to liver function is highlighted by mitochondrial dysfunction  
71 observed in inborn and acquired liver pathologies: mutations in mitochondrial genes that cause  
72 genetic diseases manifest with liver dysfunction, while strong associations also exist between  
73 mitochondrial dysfunction and acquired liver diseases such as NAFLD, viral hepatitis, and ischemic  
74 liver injury<sup>8,9</sup>. Mitochondrial respiration has been reported to decline during the progression of liver  
75 dysfunction in humans<sup>10</sup> and perturbation of mitochondrial structure has been reported in liver

76 biopsies from patients with NASH<sup>11</sup>, lending support to the notion that the maintenance of  
77 mitochondrial integrity is paramount to liver function. Promoting enhanced oxygen consumption  
78 with targeted uncouplers in the liver reduces the deleterious accumulation of hepatic lipid storage  
79 and steatosis in rodents and primates<sup>12,13</sup>, yet broader system-wide mitochondrial uncoupling has  
80 catastrophic effects on other organs and is incompatible with life<sup>14</sup>. We recently showed that  
81 mitochondrial uncoupling in cardiac mitochondria is regulated by Mitochondrial Fission Process 1  
82 (MTFP1), uncovering a novel role of this protein in bioenergetic regulation<sup>15</sup>. MTFP1 is a protein  
83 localized at the inner membrane (IMM) whose namesake derives from a putative role in  
84 mitochondrial fission in vitro<sup>16,17</sup> and has garnered interest as marker of liver dysfunction in  
85 humans. Retrospective studies revealed a link between *MTFP1* expression in tumoral tissue and  
86 patient survival in HCC<sup>18</sup>, the most common type of liver cancer, whose development is heavily  
87 influenced by NAFLD progression<sup>2</sup>. Indeed, compelling evidence implicates MTFP1 in metabolic  
88 sensing and programmed cell death regulation in vitro<sup>17,19,20</sup>, although its pertinence in the liver  
89 function and metabolism has never been explored.

90 Here, we report the generation of a liver-specific *Mtfp1* knockout mouse model (LMKO) and  
91 discover that, contrary to what we observed for the heart<sup>15</sup>, MTFP1 is dispensable for organ  
92 function. We report that deletion of *Mtfp1* in vivo in hepatocytes enhances hepatic OXPHOS  
93 activity and confers protection against diet-induced liver steatosis, weight gain and systemic  
94 glucose dysregulation when mice are fed a high fat diet (HFD). In sum, our data reveal liver-  
95 specific effects of MTFP1 ablation in vivo that position this gene as a therapeutic candidate for  
96 NAFLD.

## 97 **Results**

### 98 **Generation and characterization of liver specific *Mtfp1* KO mouse model**

99 To investigate the link between mitochondrial function and liver metabolism we generated a  
100 liver-specific KO mouse model in which we specifically deleted *Mtfp1* in post-natal hepatocytes  
101 (LMKO mice; Fig. 1A, S1A-B). Conditional mice (*Mtfp1<sup>LoxP/LoxP</sup>*) previously generated on a  
102 C57Bl6/N background<sup>15</sup> were crossed to Alb-Cre recombinase transgenic mice (*Alb-Cre<sup>tg/+</sup>*) to  
103 generate LMKO mice (*Alb-Cre<sup>tg/+</sup>Mtfp1<sup>LoxP/LoxP</sup>*). Genetic deletion of *Mtfp1* in LMKO mice was  
104 specific to the liver (Fig. 1B) and caused a profound depletion of mRNA (Fig. 1C) and protein (Fig.  
105 1D) expression in liver extracts. MTFP1 ablation in hepatocytes did not affect perinatal survival  
106 (Fig. 1E) and histological liver analysis performed on LMKO mice were unremarkable and  
107 indistinguishable from those of control littermates (Fig. 1F). Contrary to the ablation of MTFP1 in  
108 the heart<sup>15</sup>, LMKO mice did not manifest any overt defects during their lifetime under normal chow  
109 diet (NCD). Comprehensive assessment of liver structure and function revealed no defects: liver  
110 mass (Fig. 1G) was unchanged in LMKO mice and the levels of circulating biomarkers of liver  
111 damage such as alanine aminotransaminase (ALAT) and aspartate aminotransaminase (ASAT)  
112 were not increased relative to those of control littermates (Fig. 1H). Circulating levels of cholesterol  
113 and triglycerides were normal (Fig. 1I) and metabolic cage performance was not impaired (Fig. 1J-  
114 S1C). Similarly, we observed no evidence of pathological gene expression changes by RNAseq  
115 analysis (Fig. S1D, Supplemental Dataset 1). In fact, control and LMKO livers revealed virtually no  
116 gene dysregulation (only 27 out of >25,000 transcripts) including no upregulation of established  
117 markers<sup>21</sup> of NAFLD or HCC defined in humans (Fig. S1D, Supplemental Dataset 1). Taken  
118 together, our observations demonstrate that the deletion of *Mtfp1* in hepatocytes does not  
119 negatively impact the liver under basal conditions.

120

### 121 ***Mtfp1* deletion increases OXPHOS activity and mitochondrial respiration**

122 Given our previous observations that MTFP1 ablation reduces bioenergetic efficiency of  
123 cardiac mitochondria<sup>15</sup>, we decided to directly assess the impact of *Mtfp1* deletion on hepatic  
124 mitochondrial bioenergetics. To this end, we performed high resolution fluor-respirometry on  
125 isolated hepatic mitochondria isolated from control and LMKO mice, simultaneously measuring

126 both oxygen consumption rates ( $JO_2$ ) and mitochondrial membrane potential ( $\Delta\Psi$ ) changes with  
127 Rhodamine 123 (RH-123)<sup>22</sup>.  $JO_2$  and RH-123 were recorded from mitochondria incubated with  
128 respiratory substrates promoting the delivery of electrons to complex I (state 2; pyruvate,  
129 glutamate, and malate (PGM) or complex II (state 2; succinate and rotenone), and also in the  
130 presence of palmitoyl-carnitine plus malate then in the phosphorylating (state 3: ADP), non-  
131 phosphorylating (state 4: oligomycin (OLGM) to inhibit ATP synthase) (Fig. 2A). Notably, and in  
132 contrast to MTFP1-deficient cardiac mitochondria<sup>15</sup>, respiration in LMKO liver mitochondria was  
133 significantly increased in phosphorylating (state 3) conditions in the presence of any of the  
134 respiratory substrates we tested. Pyruvate, glutamate, and malate led to a 49% increase in state 3  
135 respiration and succinate and rotenone led to a 57% increase in respiration (Fig. 2B). Interestingly,  
136 we observed a 200% increase in state 3 respiration in the presence of palmitoyl carnitine, a fatty  
137 acid ester derivative, pointing to an increased efficiency of fatty-acid derived energy metabolism  
138 caused by hepatocyte-specific deletion of *Mtfp1*.

139 Additionally, LMKO liver mitochondria showed a higher respiratory control ratio (RCR) in  
140 the presence palmitoyl carnitine plus malate (Fig 2C). Despite a marked increase in state 3  
141 respiration, we did not observe a genotype-specific difference in mitochondrial membrane potential  
142 (Fig. 2D), which initially surprised us since increased oxygen consumption rates are typically  
143 accompanied by reduction in membrane potential due to dissipation of the protonmotive force via  
144 complex V (to synthesize ATP). The most parsimonious explanation for this result is that MTFP1  
145 ablation promotes a commensurate increase in the activities of both cytochrome *c* oxidase  
146 (complex IV) and the ATP synthase (complex V). Indeed, when we measured the specific activities  
147 of complex IV (Fig. 2E) and complex V (Fig. 2F) in separate assays, we found a ~20% increase in  
148 LMKO mitochondria relative to control littermate controls, suggesting a similar contribution of both  
149 complexes to increase respiration while maintaining mitochondrial membrane potential. We further  
150 confirmed our findings by measuring oxygen consumption rates in mitoplasts supplied with either  
151 NADH, Cyt *c*, succinate and rotenone to drive electron transport via Complex II or NADH, Cyt *c*,  
152 succinate and malonate to drive electron transport via Complex I (Fig. 2G). In both assays, oxygen  
153 consumption was elevated in LMKO liver mitochondria demonstrating that Complex IV activity is  
154 intrinsically augmented upon MTFP1 ablation independently of the protonmotive force. Together,

155 these observations implied either that MTFP1 ablation triggers a specific upregulation of  
156 components of the OXPHOS machinery or the induction of a general mitochondrial biogenesis  
157 response. To differentiate between these possibilities, we assessed mitochondrial mass using  
158 multiple molecular and imaging-based methods. Quantification of mitochondrial mass in primary  
159 hepatocytes isolated from control or LMKO mice expressing a genetically encoded matrix-targeted  
160 YFP (mitoYFP) showed no differences in fluorescent signal intensity or surface area (Fig. S2A B),  
161 indicating that mitochondrial mass is unaffected by MTFP1 ablation in primary hepatocytes.  
162 Interestingly, we found a modest increase in mitochondrial elongation in LMKO mitochondria (Fig.  
163 S2C) quantified by supervised machine learning<sup>23</sup>, consistent with previous studies in cultured  
164 cells<sup>15,17</sup>. Quantification of mtDNA content in liver tissue revealed no genotype-specific differences  
165 in mice fed a NCD (Fig. S2D) and transmission electron microscopy (TEM) analyses of liver  
166 sections showed no differences in mitochondrial area between control and LMKO mice (Fig. S2E).  
167 RNAseq analyses showed no evidence of gene expression signatures typically associated with  
168 increased mitochondrial biogenesis or integrated stress responses (Fig. S2E, Supplemental  
169 Dataset 1) and shotgun liver proteomics performed on control and LMKO liver extracts revealed no  
170 global upregulation of mitochondrial proteins (Fig. 1D, Supplemental Dataset 2). Taken together,  
171 our data strongly argue that a specific and coordinated increase in both complex IV and V activity  
172 in hepatocytes enhances respiration in liver mitochondria deleted of *Mtfp1*, enabling them to  
173 consume nutrient-derived respiratory substrates at an elevated rate.

174

#### 175 **MTFP1 interacts with OXPHOS-related proteins in the liver.**

176 To gain insights into the mechanisms responsible for the increased specific activities, we  
177 assessed the relative complex abundance by grouping mitochondrial proteins quantified by  
178 proteomics in the liver of NCD-fed LMKO mice according to the macromolecular complexes to  
179 which they belong (Fig. 2H, Supplemental Dataset 2). These data revealed a significant increase  
180 in Complex V subunits, which could be confirmed by quantitative SDS-PAGE (Fig. 2I) and Blue-  
181 native polyacrylamide gel electrophoresis (BN-PAGE) analyses (Fig. 2J). BN-PAGE analysis of  
182 the steady-state levels of OXPHOS complexes in LMKO liver mitochondria revealed an increase in  
183 Complex V dimers (Fig. 2J) to an increase commensurate with the reported increase in ATPase

184 activity (Fig. 2F). Taken together, our data suggest that improved assembly and/or maintenance of  
185 Complex V along with an increased activity of Complex IV is responsible for the enhanced  
186 respiration observed in LMKO liver mitochondria.

187 To gain insights into the relationship between MTFP1 and macromolecular complex  
188 assembly in the inner mitochondrial membrane (IMM), we sought to assess the interactome of  
189 MTFP1 in the liver. We generated a hepatocyte-specific transgenic mouse model enabling the  
190 expression of FLAG-MTFP1 from the *Rosa26* locus (Fig. 3A). We verified that the Hepatocyte<sup>FLAG-</sup>  
191 <sup>MTFP1</sup> mice, expressed FLAG-MTFP1 correctly in the IMM by protease protection assay (Fig. 3B).  
192 We then subjected liver mitochondria to co-immunoprecipitation (co-IP) and mass spectrometry  
193 (MS/MS) to define interacting protein partners, which enabled the identification of 112 specific  
194 interactors of MTFP1 with fold change (FC) >2 by MS/MS analysis (Figure 3C, D, Supplemental  
195 Dataset 3) that could be ascribed to the mitochondrial proteome according to the Mitocarta 3.0  
196 compendium<sup>24</sup>. We then decided to subdivide this list into binary and enriched interactors: binary  
197 interactors were those proteins we could only identify in Hepatocyte<sup>FLAG-MTFP1</sup> but not control liver  
198 mitochondria CoIP eluates while enriched interactors were those proteins for which peptide  
199 abundance was greater in CoIP eluates from Hepatocyte<sup>FLAG-MTFP1</sup> mice than in control mice.

200 Classification of binary interacting proteins revealed a wide range of mitochondrial  
201 functions, with a conspicuous abundance of factors involved in mitochondrial translation and  
202 OXPHOS (Fig. 3D). On the other hand, enriched interactors did not reveal an enrichment of  
203 proteins required for mitochondrial translation, but rather those involved in various metabolic  
204 processes within mitochondria, including carrier proteins of the SLC25A family. 2D-BN-PAGE  
205 analyses revealed the formation of an MTFP1 macromolecular complex in liver mitochondria,  
206 which was absent in LMKO mice, and that co-migrated with SLC25A4 (ANT1) (Fig. 3E), as we  
207 recently described in the heart<sup>15</sup>. However, we found little overlap with the cardiac interactome of  
208 MTFP1<sup>15</sup> (7 out of 113 proteins), implying that there may be tissue-specific physical interactions  
209 and complex assembly associated with MTFP1 beyond ANT1 that regulate respiration. Altogether,  
210 these data indicate that post-transcriptional modulation of mitochondrial gene expression and IMM  
211 complex abundance and activities are induced in a specific manner by the deletion of MTFP1 in  
212 hepatocytes, leading to enhanced mitochondrial respiration.



213

## 214 ***Mtfp1* deletion protects against hepatic steatosis induced by high fat diet**

215         Given enhanced stimulated respiratory activity of LMKO liver mitochondria, we next  
216 decided to assess the response of LMKO mice to high fat diet (HFD) feeding, a classical metabolic  
217 burden for the liver that causes nutrient overload, hepatic steatosis, and systemic metabolic  
218 dysregulation that can be counteracted by accelerating oxygen consumption via mitochondrial  
219 uncoupling<sup>12,13</sup>. We fed control and LMKO mice a HFD for a period of 16 weeks beginning at 8  
220 weeks of age, which was previously shown to drive diet-induced obesity and NAFLD<sup>25</sup>. In control  
221 mice, we observed that chronic HFD feeding triggered the hypertrophy of livers (Fig. 4A), which  
222 were appreciably paler and heavier (Fig. 4B) than those of control mice on NCD. HFD feeding  
223 also induced weight gain (Fig. 4C) and accumulation of hepatic triglycerides (TG), (Fig. 4D).  
224 Histological analyses showed a massive accumulation of lipid droplets (in white), consistent with  
225 both micro- and macro-steatosis (Fig. 4E). In contrast, HFD-fed LMKO mice were protected from  
226 weight gain (Fig. 4C) and liver dysfunction, exhibiting a 26% of reduction in liver mass compared to  
227 diet-matched controls (Fig. 4A, 4B). Concordantly, histological analyses of livers from HFD-fed  
228 LMKO mice revealed a reduction in steatosis (Fig. 4E), a complete rescue of hepatic triglycerides  
229 accumulation back to levels measured in NCD-treated mice (Fig. 4D), and a reduction in circulating  
230 levels of ALAT by 64% and ASAT by 32% (Fig. 4F). Metabolic protection against HFD-feeding in  
231 LMKO mice was reflected at the molecular level: liver RNAseq analyses showed that HFD feeding  
232 induced significant transcriptional dysregulation in control livers with 854 upregulated genes and  
233 758 downregulated genes (Fig. 4G, S3). Gene ontology analyses revealed an enrichment of  
234 various metabolic pathways dysregulated by HFD-feeding in control mice including, lipid and  
235 branched chain amino acid metabolism, PPAR signaling, and steroid biosynthesis, and fatty acid  
236 metabolism. These alterations were absent in HFD-fed LMKO mice, in which only 214 upregulated  
237 genes and 164 downregulated genes were detected, most of which were involved in pathways of  
238 stress response and immune signaling (Fig. 4H). At the protein level, we observed that in HFD  
239 feeding in control mice induced global reduction in complex IV by liver proteomic analyses (Fig.  
240 S4A). This response was blunted in LMKO mice (Fig. S4B), leading to a relative increase in

241 complex IV proteins in HFD-fed LMKO mice compared to littermate, diet-matched controls (Fig.  
242 S4C).

243         Given the protection against hepatocyte and liver damage observed in vivo and in vitro  
244 upon the deletion of *Mtfp1*, we asked whether the protection against HFD-induced metabolic  
245 dysregulation of the liver could be explained by differential sensitivity to cell death. However,  
246 TUNEL assays performed on histological sections from HFD-fed control and LMKO mice revealed  
247 an absence hepatocyte apoptosis (Fig. 4I), which is consistent with previous findings that HFD  
248 causes limited liver cell death<sup>25</sup>. Altogether, our data demonstrate that *Mtfp1* deletion in  
249 hepatocytes confers metabolic resistance to hepatic steatosis in vivo (Fig. 4J) in a manner that is  
250 independent of apoptotic resistance.

251

#### 252 ***Mtfp1* deletion improves hepatocyte metabolism in a cell-autonomous.**

253         Having demonstrated that LMKO mice are protected against diet-induced steatosis, we  
254 next sought to define the breadth of systemic protection by performing a battery of metabolic tests  
255 on control and LMKO mice after HFD-feeding. Fat accumulation is known to affect systemic  
256 glucose homeostasis. Consistent with improved liver metabolism promoted by the ablation of  
257 MTFP1 in hepatocytes, metabolic cage analyses revealed improved systemic respiration in LMKO  
258 mice fed an HFD. The lower respiratory exchange ratio (RER) observed in LMKO mice (Fig. 5A)  
259 suggests that LMKO mice metabolize nutrient-derived lipids more efficiently than control  
260 littermates, which can very likely be attributed to intrinsic differences in the livers of these mice.  
261 Food and water intake were not altered between control and LMKO mice nor were distance  
262 measurement on HFD (Fig. S5A-C), pointing to a specific effect of MTFP1 on energy expenditure  
263 by the liver that is revealed under HFD feeding. Metabolic dysregulation caused by HFD feeding is  
264 known to increase *de novo* glucose synthesis by the liver of rodents<sup>27</sup> and so we sought to assess  
265 gluconeogenesis by performing intraperitoneal pyruvate tolerance tests (IP-PTT). We observed a  
266 1.5-fold increase blood glucose levels in HFD-fed control mice relative to NCD littermates, which  
267 was reduced by 14% in the HFD-fed LMKO group (Fig. 5B), indicating that *Mtfp1* deletion in  
268 hepatocytes protects the liver against diet-induced dysregulation of gluconeogenesis. Consistent  
269 with these findings, intraperitoneal glucose tolerance tests (IP-GTT) revealed LMKO mice to be

270 modestly protected from HFD-induced glucose intolerance. In control mice, HFD feeding led to a  
271 1.7-fold increase of the area under curve (AUC) of IP-GTT relative to normal chow diet (NCD)  
272 controls, which reduced by 17% in HFD-fed LMKO mice relative to diet-matched controls (Fig. 5C).  
273 To exclude that improved glucose tolerance in HFD-fed LMKO mice was the consequence of  
274 altered insulin resistance, rather than improved gluconeogenesis, we performed intraperitoneal  
275 insulin tolerance tests (IP-ITT). We observed no genotype-specific differences in insulin sensitivity  
276 (Fig. 5D) on either HFD or NCD, indicating that improved glucose tolerance in LMKO mice is not  
277 caused by increased systemic insulin sensitivity. Concordantly, we did not observe differences in  
278 basal insulin levels between control and LMKO mice fed a NCD (Fig S5E). While LMKO mice  
279 gained less weight upon HFD feeding (Fig. 4C), we observed no genotype-specific differences in  
280 body mass composition by NMR minispec analysis (Fig. 5E) nor in the circulating levels of  
281 cholesterol and triglycerides (Fig. 4F). In line with these findings, LMKO mice were not protected  
282 from extra-hepatic fat mass accumulation (Fig. 5G), white adipose tissue accumulation nor  
283 adipocyte hypertrophy (Fig. S5E, F), all of which are common metabolic consequences of diet-  
284 induced obesity<sup>17,19,28</sup>. Altogether, our data demonstrate that the protection against diet-induced  
285 metabolic dysregulation conferred to mice by hepatocyte-specific deletion of *Mtfp1* is primarily  
286 restricted to the liver.

287 To determine whether hepatocyte deletion of *Mtfp1* prevents steatosis in a cell-autonomous  
288 manner, we established an assay in which we could mimic HFD-induced steatosis in primary  
289 hepatocytes isolated from NCD-fed mice. Primary hepatocytes were plated and cultured in the  
290 presence of Intralipid (IntLip): a complex lipid emulsion composed of linoleic, oleic, palmitic, and  
291 stearic acids, which are the most abundant fatty acids found in HFD. We optimized our assay  
292 conditions to ensure that limited damage, death, or differentiation under both treated and non-  
293 treated (NT) conditions was occurring. Indeed, IntLip feeding of primary hepatocytes isolated from  
294 NCD-fed control mice led to a 1.6-fold increase in intracellular lipid accumulation after 24 hours,  
295 which could be visualized by live-cell imaging with BODIPY fluorescence (Fig. 5H) and quantified  
296 by high-throughput confocal imaging (Figure 5I). Notably, deletion of *Mtfp1* in primary hepatocytes  
297 rescued this phenotype: BODIPY staining intensities in NT and IntLip-treated *Mtfp1*<sup>-/-</sup> cells were  
298 indistinguishable to those of NT primary hepatocytes isolated from control littermates. Thus, we

299 conclude that the deletion of *Mtfp1* in hepatocytes confers direct protection to the liver against  
300 HFD-induced metabolic dysregulation by improving hepatocyte metabolism in a cell-autonomous  
301 manner.

302

### 303 ***Mtfp1* deletion protects against hepatic cell death**

304 Given the previous implications of MTFP1 in cell death sensitivity reported in various  
305 cultured cell lines<sup>17,19,28</sup> and the association of MTFP1 and liver tumor progression in humans<sup>29</sup>, we  
306 sought to directly test whether MTFP1 was involved in the regulation of cell survival in vivo. We  
307 measured the response to liver apoptosis by treating 3 month old mice for 24 hours with FAS  
308 antibodies, which specifically induces apoptotic liver damage via the activation of the FADD  
309 signaling pathway in a manner than is regulated by IMM integrity<sup>30</sup>. Macroscopically, the livers of  
310 WT mice treated with FAS showed hepatic damage characterized by the appearance of fibrotic  
311 and necrotic foci (Fig. 6A). FAS-induced liver damage resulted in a loss of liver mass (Fig. S6A), a  
312 dramatic increase of ALAT, ASAT and lactate dehydrogenase (LDH), a more general marker of  
313 tissue damage, by 35, 85 and 45-fold respectively in control livers (Fig. 6B, S6B). Hematoxylin  
314 and eosin (H&E) staining of control livers revealed tissue disruption, characterized by the presence  
315 of apoptotic bodies and hyper-eosinophilic cytoplasm, conferring large areas of architecture  
316 dysregulation (Fig. 6C), all of which features are consistent with apoptotic liver damage<sup>15,23</sup>. In  
317 contrast, H&E analyses of LMKO livers revealed far less FAS-induced damage (Fig. 6C) and  
318 plasma analyses revealed an 84% reduction of ALAT, an 86% reduction of ASAT, and a 97%  
319 reduction of LDH compared to FAS-injected control mice (Fig. 6B, Fig. S6B). Finally, TUNEL  
320 assays performed on histological liver sections demonstrated a profound reduction of cell death in  
321 FAS-treated LMKO mice compared to control mice (Fig. 6D). Taken together, these studies  
322 demonstrate that hepatocyte-specific *Mtfp1* depletion protects against apoptosis-induced liver  
323 damage in vivo.

324 To understand whether MTFP1 ablation protects hepatocytes from cell death in a cell-  
325 autonomous manner, we isolated primary hepatocytes from control and LMKO mice at 8-10 weeks  
326 of age and performed quantitative cell death assays ex vivo. To induce cell death, primary  
327 hepatocytes were treated with hydrogen peroxide (H<sub>2</sub>O<sub>2</sub>) [1mM] at 16 hours post plating and cell

328 death was by kinetically monitored by propidium iodide (PI) uptake using an automated live-cell  
329 imaging approach powered by supervised machine learning previously developed for cultured cell  
330 lines<sup>31,32</sup>. Consistent with our observations in vivo, *Mtfp1*<sup>-/-</sup> primary hepatocytes treated with H<sub>2</sub>O<sub>2</sub>  
331 ex vivo showed a significant resistance against cell death (52% reduction at 4 hours) compared to  
332 control primary hepatocytes (Fig. 6E, F), arguing that MTFP1 ablation confers protection to  
333 autonomous hepatocyte death ex vivo. Programmed cell death in the liver, and more specifically  
334 in hepatocytes, can be tightly regulated through the opening of the mitochondrial permeability  
335 transition pore (mPTP)<sup>32</sup>. To test whether *Mtfp1* deletion impacted mPTP opening, we isolated  
336 hepatic mitochondria and simulated mPTP opening with calcium chloride overload (Fig. 6G). We  
337 observed a reduced sensitivity of mPTP opening in hepatic mitochondria isolated from LMKO mice  
338 compared to control littermates (Fig. 6G), which could be rescued by the pre-treatment with the  
339 mPTP inhibitor Cyclosporin A (CsA)<sup>19</sup>. Taken together, we conclude that *Mtfp1* deletion in  
340 hepatocytes confers protection against mPTP opening and cell death induction.

341

## 342 **Discussion**

343 Pre-clinical transgenic animal models have been instrumental in dissecting the underlying  
344 molecular remodeling of hepatocytes during the development of fatty liver disease and its  
345 sequelae. These studies have demonstrated the unassailable pathophysiological relevance of  
346 mitochondria, yet data from a large array knockout mice of mitochondrial genes have yielded a  
347 more complex picture: some hepatocyte-specific knockouts confer resistance to NAFLD/NASH  
348 while others inhibit normal liver function<sup>33-37</sup>. Pleiotropic effects of the individual mitochondrial  
349 genes that were targeted in previous studies combined with the potential for metabolic cross-talk  
350 between tissues in vivo has made it challenging to pinpoint how modulating mitochondrial activity  
351 may be used to combat liver disease. Here, we discovered that Mitochondrial Fission Process 1  
352 (MTFP1) plays an important role metabolic role in the liver of mice that is critical for NAFLD but not  
353 under basal conditions. MTFP1 was first identified as a metabolically-regulated inner mitochondrial  
354 membrane IMM) protein<sup>16-18,33</sup> initially implicated in mitochondrial fission and cell death resilience  
355 in a variety of cell lines<sup>16-18,38</sup>. In the liver, the discovery that MTFP1 protein expression is

356 predictive of hepatocellular carcinoma survival and recurrence risk in humans<sup>15</sup>, prompted us to  
357 directly investigate its role in the liver.

358 Here, we created Liver-specific *Mtfp1* knockout (LMKO) mice (Fig. 1A-E, S1A,B) by expressing a  
359 hepatocyte-specific Cre-recombinase<sup>39</sup> in a conditional mouse model of *Mtfp1*<sup>15</sup>. We discovered  
360 that LMKO mice are healthy and virtually indistinguishable from littermate control mice, showing no  
361 defects in liver function and no indication of liver damage nor inflammatory responses and liver  
362 RNAseq analyses only showed 0.1% of genes this were dysregulated, none of which were involved in  
363 pathogenic hepatic remodeling (Fig. 1, S1). While the livers of LMKO mice appeared unchanged,  
364 characterization of hepatic mitochondria revealed two major functional improvements: increased  
365 respiratory capacity and resistance to permeability transition pore opening. High resolution fluor-  
366 respirometry measurements of MTFP1-deficient liver mitochondria showed increased ADP-  
367 stimulated (state 3) oxygen consumption rates under all substrates we tested, which was  
368 associated a commensurate increase in the specific activities of complex IV and complex V (Fig.  
369 2B-F). Quantitative label-free proteomic studies revealed a ratio-metric increase in the levels of  
370 Complex V subunits, which paralleled the increased levels of assembled Complex V detected by  
371 BN-PAGE, pointing to an increased assembly and/or maintenance of the ATP synthase complex  
372 (Fig. 2G-I). Enhanced respiration was not associated with proton leak (Fig. 2B,C) nor cristae  
373 alterations (Fig. S2D) that we reported in MTFP1-deficient hearts<sup>34</sup>, leaving us wondering: how  
374 does MTFP1 ablation enhance OXPHOS activity and mitochondrial coupling and do so specifically  
375 in the liver?

376 The spare respiratory capacity of hepatocytes has been reported to supersede that of  
377 cardiomyocytes, indicating that under basal conditions cardiomyocyte mitochondria are working far  
378 closer to their maximal capacity<sup>40</sup>. In contrast, morphometric studies of cardiac mitochondria from  
379 rodents reveal cristae densities that approach the physical and functional limits exemplified by  
380 tuna<sup>41</sup> and hummingbird hearts<sup>42</sup>, consistent with the notion that there may be little additional IMM  
381 real estate upon which to build additional OXPHOS complexes in the heart<sup>43</sup>. In the liver,  
382 mitochondria have a comparatively reduced IMM density, OXPHOS protein content<sup>44</sup>, and IMM  
383 protein half-lives<sup>45</sup> and would therefore be capable of increasing OXPHOS complex assembly to  
384 enhance mitochondrial coupling and respiration. In rodents, systemic thyroid hormone injections

385 can increase hepatocyte cristae density to increase the content and activity of the respiratory  
386 chain<sup>46,47</sup>. On the other hand, genetic models of obesity manifest the opposite effect, with altered  
387 cristae organization in swollen mitochondria and reduced levels of cytochrome c oxidase<sup>48</sup>, which  
388 we also confirmed by proteomic studies of HFD-fed control mice (Fig. S4A, B). Yet to the best of  
389 our knowledge, LMKO mice represent the first genetic mouse model that elevates respiration by  
390 increasing the activity of Complex IV and V rather than by boosting total mitochondrial mass or by  
391 promoting uncoupling.

392 MTFP1 ablation in the liver enhances state 3 respiration regardless of the substrate source  
393 (Fig. 2B) yet this increase is most profound when the palmitoyl-carnitine is supplied in excess, as  
394 evidenced by the increased respiratory control ratio (RCR) in the presence of fatty acids but not  
395 carbohydrate-derived substrates (Fig. 2B), revealing that MTFP1-deficient liver mitochondria are  
396 capable of coupling voracious beta enhanced OXPHOS activity. A clear prediction of increased  
397 beta oxidation capacity of hepatocyte mitochondria is an enhanced propensity to metabolize  
398 excess lipids and therefore a resistance against diet-induced hepatic steatosis *in vivo*<sup>1</sup>. Indeed,  
399 when we challenged LMKO mice with a long-term a high fat diet (HFD), they showed remarkable  
400 resistance to fatty liver disease and metabolic dysregulation despite equal levels of food  
401 consumption and in-cage activity. Metabolic protection appears to be restricted to the liver, as  
402 LMKO mice were not protected against the increased extra-hepatic adiposity, dysregulated  
403 systemic glucose metabolism, and aberrant glucose-stimulated insulin secretion by the pancreas  
404 that caused by HFD feeding. Mimicking diet-induced steatosis in the tissue culture dish with  
405 primary hepatocytes isolated from NCD-fed mice, we could show that excessive lipid droplet  
406 accumulation was blunted in *Mtfp1*<sup>-/-</sup> primary hepatocytes *ex vivo* that is consistent with enhanced  
407 mitochondrial coupling in these cells (Fig. 5H).

408 The discovery that MTFP1 ablation in the liver is benign and even beneficial under stress  
409 conditions is in stark contrast to our recent report that *Mtfp1* deletion in cardiomyocytes causes  
410 heart failure<sup>43</sup>. However, defects in inner membrane integrity observed in *Mtfp1*<sup>-/-</sup> cardiac  
411 mitochondria were not observed in *Mtfp1*<sup>-/-</sup> liver mitochondria: membrane potential was maintained  
412 (Fig. 2C) and mPTP was increased rather than decreased (Fig. 6G). Moreover, the livers of LMKO  
413 mice show increased mitochondrial respiratory capacity (Fig. 2B) and no signs of cell death or

414 inflammation (Fig. 4I, S3A), while MTFP1 deficiency in the heart triggered cardiomyocyte death,  
415 fibrotic remodeling, and heart failure<sup>15</sup>. At first, we found these physiological discrepancies  
416 perplexing, since the heart and liver are both rely heavily on mitochondria yet further exploration of  
417 the literature provided conspicuous examples demonstrating that these two organs can in fact  
418 respond differently to mitochondrial dysfunction. For example, ablation of Complex I activity in the  
419 cardiomyocytes can cause a fatal hypertrophic cardiomyopathy in mice<sup>49</sup> while its ablation in  
420 hepatocytes does not impact liver structure and function<sup>37</sup>. Similarly, interfering with the activity of  
421 the mitochondrial fusion proteins OPA1<sup>50,51</sup> or Mitofusins<sup>52</sup> specifically in cardiomyocytes yields  
422 disastrous outcomes for cardiac function, yet in doing so in the liver is either benign<sup>33,34</sup> or even  
423 advantageous against NASH<sup>35</sup>. Similarly, cardiac deletion of the adenine nucleotide transporter  
424 elicits cardiac hypertrophy but in the liver, its genetic or biochemical inhibition in the liver can be  
425 beneficial, protecting against hepatic steatosis and metabolic dysregulation<sup>36,53</sup>. In mice, system-  
426 wide disruption of mitochondrial genes such as *Chchd10*<sup>54,55</sup>, *Dnm1f*<sup>56</sup>, *Wars2*<sup>57</sup>, and *Cox1*<sup>58</sup> can  
427 trigger multi-organ dysfunction in which the liver, but not the heart, is spared, further illustrating that  
428 the liver may respond differently (or not at all) to genetic insults otherwise catastrophic to other  
429 tissues.

430 But why does the ablation of MTFP1 impact liver mitochondria so differently? It is likely that  
431 divergent cell type-specific effects reflect the different metabolic, structural, and functional  
432 characteristics of mitochondria they harbor. Indeed, compelling differences between the heart and  
433 liver have been documented at the level of mitochondrial network morphology, IMM and cristae  
434 organization<sup>59</sup>, mitochondrial proteome composition and protein half-lives<sup>45</sup>, OXPHOS complex  
435 organization and assembly<sup>60</sup>, substrate utilization and enzymatic activities of the respiratory  
436 chain<sup>60,61</sup>, and even the molecular regulation of the mPTP<sup>61-65</sup>. Consistent with these observations,  
437 we found little overlap between the differentially expressed mitochondrial genes and proteins of  
438 knockout hearts and livers: no genes besides *Mtftp1* were commonly dysregulated between both  
439 knockout tissues while only 13% (35 out of 264 proteins) shared common differential expression  
440 patterns (Fig. S7). MTFP1 interactomes were also remarkably dissimilar, with only 7 out of 113  
441 interacting partners of liver MTFP1 found to overlap with the cardiac MTFP1 interactome. MTFP1  
442 is devoid of conserved motifs or catalytic domains and forms a complex of approximately 150kDa,



443 which is significantly smaller than the fully assembled mito-ribosome and ATP synthase complexes  
444 with whose subunits it interacts and thus we posit that the impacts on mitochondrial function that  
445 result from the ablation MTFP1 may reflect its role as a protein scaffold in the IMM. Indeed,  
446 MTFP1 co-migrates with both adenine nucleotide translocase (ANT1) and Cyclophilin D (encoded  
447 by *Ppif*), both of which have been previously physically and functionally connected to mitochondrial  
448 ATP synthesis<sup>62–66</sup> and the mPTP. Our data also support a role for MTFP1 as a regulator of mPTP  
449 activity in the liver, as inactivation of hepatocytes slows mPTP opening response in liver  
450 mitochondria and protects against liver cell death in primary hepatocytes and in mice (Fig. 6). This  
451 pro-survival role of MTFP1 in the liver appears to be independent from the metabolic protection its  
452 deletion confers against HFD-induced hepatic steatosis, since HFD-feeding does not cause cell  
453 death (Fig. 4I).

454 The metabolic protection conferred to MTFP1-deficient livers that are already hyper-  
455 proficient in mitochondrial respiration and fatty acid oxidation is best appreciated under chronic  
456 HFD feeding. Intriguingly, recombinant inbred mouse models that are susceptible to  
457 NAFLD/NASH show a downregulation of *Mtfp1* expression in the liver while those that are resistant  
458 do not<sup>67</sup>. While diet-induced hepatic steatosis predisposes humans to NASH and cirrhosis, HFD-  
459 feeding alone does trigger NASH in laboratory mice so we have not yet learned whether LMKO  
460 mice are protected from the downstream sequelae of hepatic steatosis. Nevertheless, LMKO  
461 mice have availed themselves to be a unique tool to understand how enhancing mitochondrial  
462 respiration can combat metabolic liver disease and will undoubtedly prove useful for the in vivo  
463 exploration and development of therapeutic targets for other inherited and acquired liver diseases.

464

## 465 **Materials and Methods**

### 466 ***Animals***

467 Animals were handled according to the European legislation for animal welfare ([Directive](#)  
468 [2010/63/EU](#)). All animal experiments were performed according to French legislation in  
469 compliance with the European Communities Council Directives (2010/63/UE, French Law 2013-  
470 118, February 6, 2013) and those of Institut Pasteur Animal Care Committees (CETEA is Comité

471 d'Ethique en Expérimentation Animale 89). The specific approved protocol number is #20687-  
472 2019051617105572. Mice were housed within a specific pathogen free facility and maintained  
473 under standard housing conditions of a 14-10h light-dark cycle, 50-70% humidity, 19-21°C with  
474 free access to food and water in cages enriched with bedding material and gnawing sticks. Alb-  
475 Cre recombinase<sup>39</sup> and mitoYFP<sup>68</sup> mouse lines are commercially available (MGI: 2176946 and  
476 5292496). The *Mtfp1* conditional mouse model<sup>68</sup> was generated by PolyGene on a C57Bl/6N  
477 genetic background using two LoxP sites and an FRT-flanked neomycin cassette. The first LoxP  
478 site and neomycin resistance cassette is located in intron 1 and the second LoxP site is inserted in  
479 intron 3. The FRT-flanked neomycin cassettes were removed *in vivo* by Flp-recombination by  
480 crossing to Flp-deleter breeding step. Hepatocyte specific FLAG-MTFP1 Knock-In (KI) mice (*Alb-*  
481 *Cre<sup>tg/+</sup>Mtfp1<sup>+/+</sup>, CAG<sup>tg/+</sup>*) were generated by crossing an inducible mouse model for mCherry-P2A-  
482 FLAG-MTFP1<sup>69</sup> generated by PolyGene AG (Switzerland) on a C57Bl6/N background expression  
483 under the CAG promoter with mice expressing the Cre recombinase under the control of the  
484 hepatocyte-specific albumin Cre promoter. Liver specific *Mtfp1* knockout mice (LMKO) were  
485 generated by mating AlbCre+ mice with *Mtfp1<sup>LoxP/LoxP</sup>* mice, this led to the deletion of flanked region  
486 containing exons 2 and 3 (925 bp in total), resulting in the loss of the majority of the coding region  
487 of *Mtfp1* and a loss of *Mtfp1* expression. For fluoresce microscopy analysis of primary hepatocytes  
488 the triple transgenic line AlbCre+; mitoYFP+; *Mtfp1<sup>LoxP/LoxP</sup>* was generated.

489 Mice were fed a normal chow diet (NCD, Teklad global protein diet; 20% protein, 75%  
490 carbohydrate, 5% fat) or high fat diet (HFD) containing 22 kJ% carbohydrates 24 kJ% protein and  
491 54 kJ% fat (Ssniff® EF acc. E15742-347) for 16 weeks starting from the age of 8 weeks. During  
492 the treatment mice were monitored weekly for the body weight and every other week for the  
493 glycaemia, which was measured using a glucometer (Accu-Chek Performa, Roche, 1486023). To  
494 induce hepatic cell death, Fas antigen, CD95 (BD BioSciences, 554254) was intra-peritoneal  
495 injected in 18-hour fasted mice at the concentration of 225µg/kg (BW). Mice were sacrificed 24  
496 hours post injection.

497 Mouse genotype was determined at weaning. For the genotyping, genomic DNA was isolated from  
498 mouse tail snip using lysis buffer Tris-HCl (EuroMedex, 26-128-3094-B) pH8.5 100mM;  
499 Ethylenediaminetetraacetic acid (EDTA, 5mM; EuroMedex, EU0084-B); Sodium Dodecyl Sulfate

500 (SDS, 0.2%; EuroMedex, 1833); Sodium Chloride (NaCl, 200mM; EuroMedex, 1112-A );  
501 Proteinase K 400 $\mu$ g/ml (Sigma-Aldrich, 03115879001); samples were incubated at 56°C until  
502 digested and then centrifuged for 3 min at 16000g. Supernatants were transferred to fresh tubes,  
503 and DNA was precipitated first with 1000  $\mu$ l of isopropanol, centrifuged at 16000g for 10 minutes at  
504 4°C, pellet were washed with 500  $\mu$ l of 70% ethanol, centrifuged at 16000g for 10 minutes at 4°C,  
505 and DNA was resuspended in H<sub>2</sub>O. PCR was performed using the 5x Hot FIREpol (SOLIS  
506 BIODYNE, 755015) at 94°C for 3 minutes, (94°C for 15 seconds, 55°C 30 seconds, 72°C for 1  
507 minute) for 35 cycles, 72°C for 7 minutes and 4°C. Primers used for genotyping are listed in  
508 Supplemental Dataset 4.

### 509 ***Metabolic studies***

510 Food and water intake, respiratory exchange ratio (RER), and physical activity were tested for 5  
511 days using the PhenoMaster system (TSE Systems, Bad Homburg, Germany), which allowed  
512 continuous undisturbed and controlled recording. during day and night periods. 5 days before the  
513 recording, the animals were placed in the room and in cages similar to the PhenoMaster cages, for  
514 acclimatization. The following parameters were recorded every 3 minutes and averaged hourly or  
515 for the light and dark phase as indicated: food consumption (g), water consumption (ml), distance  
516 covered (cm), and RER (ratio between the amount of carbon dioxide (CO<sub>2</sub>) produced in  
517 metabolism and oxygen (O<sub>2</sub>) used). RER has a range from 0.7 to 1.0 according to the fuel source,  
518 when close to 0.7 means that fats are the predominant source, closest to 1.0, carbohydrates are  
519 predominantly consumed.

520 For Pyruvate Tolerance Test (IP-PTT): 18-hour fasted mice were administered intra-peritoneal  
521 injections of sterile pyruvate (Sigma-Aldrich, P2256) at 1 g/kg (BW). Glucose and Insulin Tests for  
522 Glucose Tolerance Test (IP-GTT): 18-hour fasted mice were administered intra-peritoneal  
523 injections of sterile glucose (EuroMedex, UG3050) at 2 g/kg. For Insulin Tolerance Test (IP-ITT): 6-  
524 hour fasted mice were administered intra-peritoneal injections of Insulin aspart (NovoRapid) at 1  
525 g/kg (BW). For all the tests, blood glucose levels were measured before injection and 15, 30, and  
526 60 post-injection using a glucometer (Accu-Chek Performa, Roche). For glucose-stimulated insulin  
527 production, mice were fasted for 18 hours and were administered intra-peritoneal injections of

528 sterile glucose (EuroMedex, UG3050) at 2 g/kg. Insulin levels were analyzed by ELISA (Crystal  
529 Chem, 90082).

530 Whole blood was collected from the submandibular vein of awake mice in tubes containing heparin  
531 (Sigma-Aldrich, H4784) at the concentration of 50U/ml and centrifuged at 3000g for 10 minutes at  
532 4°C to isolate plasma. Plasma analyses of transaminases (ASAT and ALAT), LDH, cholesterol and  
533 triglycerides (TG) were performed by the 'Microdosages biochimiques' at the 'Institut de  
534 Physiologie et Pathologie, Claude Bernard' core facility (Paris).

### 535 ***Analysis of body composition***

536 Fat and lean mass were determined in awake Control and LMKO mice by nuclear magnetic  
537 resonance (NMR) using the Contactless Check Weighing (CCW) by MiniSpec MQ (Bruker  
538 MiniSpec Plus) with a 0.15-T magnetic field and a 6.2-MHz frequency pulse. This device measures  
539 the mass of fat, lean tissue, and fluid based on prior calibration. Mice were placed in an acrylic  
540 cylinder (48-mm diameter) and was loosely restrained within the cylinder by pushing a plunger.  
541 The cylinder was then positioned inside the bore of the magnet maintained at constant  
542 temperature of 37°C. The measurements were recorded as % of fat, lean, and fluids.

### 543 ***Tissue analyses***

544 Histological and morphometric analysis: liver and white adipose tissue were fixed with phosphate-  
545 buffered 10% formalin (Sigma-Aldrich, F5554) for 20 hours then washed in 70% ethanol, then  
546 embedded in paraffin, sectioned by microtome (4 um) and stained with hematoxylin & eosin. Cell  
547 death was assessed using the TUNEL assay kit – HRP – DAB (AbCam, ab206386). All slides were  
548 scanned using the Slide scanner Axio Scan.Z1 (ZEISS). Representative pictures were obtained  
549 using the CZI software (Zen 2.3 lite; ZEISS).

550 Triglyceride assay: snap frozen liver tissue was used to assess hepatic triglyceride content by  
551 fluorometric assay (AbCam, ab178780).

### 552 ***Isolation of mitochondria***

553 Livers were gently homogenized on ice in Mitochondria Isolation Buffer (MIB: Sucrose 275mM  
554 (EuroMedex, 200-301-b); ethylene glycol tetra acetic acid (EGTA-KOH pH7 1mM; EuroMedex,

555 E4378) Tris pH 7.4 20mM; Bovine Serum Albumin (free fatty acid BSA, 0.25 mg/ml; Sigma-Aldrich,  
556 A6003) and protease inhibitors (Roche). Differential centrifugation at 1000g for 10 minutes at 4°C  
557 yielded supernatant that was subsequently centrifuged at 3000g for 15 minutes at 4°C. The  
558 resulting crude mitochondrial pellet fraction was resuspended in MIB and protein concentration  
559 was quantified with Bradford assay (Sigma-Aldrich, B6916) using a spectrophotometer (Infinite 200  
560 Pro, Tecan). Isolated mitochondria were used for Blue-Native Polyacrylamide Gel Electrophoresis  
561 (BN-PAGE), SDS-PAGE or for High-Resolution Respirometry (HRR) assays.

### 562 ***High Resolution Respirometry***

563 Mitochondrial oxygen consumption was measured with an Oxygraph-2k (Oroboros Instruments,  
564 Innsbruck, AT). 50 to 500 µg of mitochondria were diluted in 2.1 ml of mitochondrial respiration  
565 buffer (Magnesium Chloride (MgCl<sub>2</sub>, 3mM; Sigma-Aldrich, M3634); Lactobionic Acid 60mM  
566 (Sigma-Aldrich, 153516); Taurine 20mM (Sigma-Aldrich, T0625); Potassium phosphate monobasic  
567 (KH<sub>2</sub>PO<sub>4</sub>, 10mM; EuroMedex, 2018); 4-(2-Hydroxyethyl)piperazine-1-ethanesulfonic acid, N-(2-  
568 Hydroxyethyl)piperazine-N'-(2-ethanesulfonic acid) (HEPES-KOH pH 7.4 20 mM; EuroMedex, 10-  
569 110); Sucrose 110mM; EGTA-KOH pH7 0.5mM and free fatty acid BSA 1g/l). To ensure  
570 mitochondrial quality and integrity, cytochrome *c* (CytC, 2µM;Sigma-Aldrich, C7752) was used.  
571 The oxygen consumption (JO<sub>2</sub>) rate was measured using either Pyruvate 10mM, Glutamate 5mM  
572 (Sigma-Aldrich, G1626) and Malate 5mM (Sigma-Aldrich, M1000), or Palmitoyl-Carnitine (PC,  
573 25µM; Sigma-Aldrich, P1645). To specifically assess Complex II activity, Rotenone 0.5 µM (Sigma-  
574 Aldrich, R8875) and Succinate 10mM (Sigma-Aldrich, S2378) were used as substrates. Oxygen  
575 consumption was assessed in the phosphorylating state with Adenosine 5'-diphosphate  
576 monopotassium salt dihydrate (ADP, 0.2 mM; Sigma-Aldrich, A5285) or non-phosphorylating state  
577 by adding oligomycin (OLGM, 5 µM, Sigma-Aldrich, O4876).  
578 The cytochrome *c* oxidase (COX) activity was measured in the presence of Ascorbate-Na (2mM;  
579 Sigma-Aldrich, A4034; pH6 with Ascorbic acid (Sigma-Aldrich, A7506)) and N,N,N',N'-Tetramethyl-  
580 p-phenylenediamine dihydrochloride (TMPD, 0.5mM; Sigma-Aldrich, 87890), with prior inhibition  
581 with Antimycin A (AMA, 2,5µM; Sigma-Aldrich, A8674), finally KCN (2mM, Sigma-Aldrich, 60178)  
582 was injected to evaluate the effective complex IV-dependent respiration.

583 The ATPase activity was assessed by colorimetric assay. Mitoplasts were incubated for 15  
584 minutes in the following buffer: triethanolamine 75mM (Sigma-Aldrich, T58300), MgCl<sub>2</sub> 2mM pH8.9  
585 followed by the addition of ATP 5mM (Sigma-Aldrich, A6419) or ATP 5mM and Oligomycin 5μM (to  
586 determine the oligomycin-insensitive ATPase activity) or ADP 5mM (used as negative control).

587

#### 588 ***Mitochondrial swelling assay***

589 Mitochondrial permeability transition pore opening was monitored by calcium-induced  
590 mitochondrial swelling and change of light scattering (absorbance 540 nm). Freshly isolated  
591 hepatic mitochondria from control and LMKO mice aged 8-10 week were resuspended in Ca<sup>2+</sup>  
592 uptake buffer (120mM KCl, 5mM MOPS, 5mM KH<sub>2</sub>PO<sub>4</sub>, 10mM Glutamate, 5mM Malate, pH 7.4 in  
593 presence of cComplete™ EDTA-free Protease Inhibitor Cocktail (Sigma 4693132001) at a  
594 concentration of 500 μg/mL and stimulated by the addition of a single pulse of 125μM CaCl<sub>2</sub>. The  
595 absorbance at 540 nm was measured at intervals of 30 seconds for 20 minutes at 37°C using the  
596 microplate reader (Tecan). Cyclosporin A (1μM) was used to inhibit the mPTP opening.

#### 597 ***BN-PAGE of liver mitochondria***

598 1D BN-PAGE was performed as described previously<sup>69</sup> with some modifications. Briefly, liver  
599 mitochondria (100 μg, mitochondrial protein concentration was determined with DC Protein Assay  
600 BIO-RAD) were isolated from control and LMKO mice and incubated with digitonin extraction buffer  
601 (HEPES (30mM), potassium Acetate (150 mM), Glycerol (12%), 6-Aminocaproic acid (2mM),  
602 EDTA (2mM), high purity digitonin (4.5g/g), pH=7.2). Mitochondria were vortexed 1 hour at 4°C to  
603 solubilize membranes and after centrifugated at 21,000 g for 30 minutes. Supernatants were  
604 transferred to a new tube and mixed with loading dye (0.0124% (w/v), Coomassie brilliant blue G-  
605 250 (Invitrogen, BN2004)). Digitonin solubilized mitochondria were loaded 3-12% Bis-Tris  
606 Invitrogen™ Novex™ NativePAGE™ 3-12% acrylamide gel (1mm) (Invitrogen, BN2011BX10)  
607 using the anode running buffer (Invitrogen, BN2001) and Cathode Buffer Additive (0.5%) added to  
608 the anode buffer (Invitrogen, BN2002). Samples were migrated at 80V 20mA for 45 minutes and at  
609 150V 20 mA for 13 hours. Gel was incubated in Transfer buffer (Tris (0.304% w/v), Glycine (1.44%  
610 w/v)) plus SDS (0.2% v/v) and β-mercaptoetanol (0.2% v/v) for 30 minutes at room temperature

611 (RT) to denature proteins. After the incubation, gels were transferred on polyvinylidene difluoride  
612 (PVDF) in transfer buffer (Tris (0.304% w/v), Glycine (1.44% w/v), Ethanol (10%v/v)) at 400mA  
613 20V for 3 hours and 30 minutes. After transfer, membranes were washed with methanol to remove  
614 Coomassie blue staining. For immunodetection, membranes were blocked with 5% milk in Tween-  
615 Tris-buffered saline (TTBS) for 1 hour at RT and incubated overnight with the specific primary  
616 antibody diluted in blocking solution. The membrane was washed three times in TTBS and  
617 incubated for 2 hours at RT with the appropriate secondary antibody conjugated with horseradish  
618 peroxidase (HRP). Finally, membranes were incubated in Tris-HCL (0.1 M pH 8.5) plus Luminol  
619 and p-Coumaric acid for 3 minutes and luminescence was detected using a ChemiDoc TM  
620 XRS+Imaging System. Band intensity was determined with Image Lab Software  
621 For 2D BN-PAGE, first dimension native gels were incubated in MOPS1x SDS Running Buffer  
622 (Fished Scientific) supplemented with  $\beta$ -mercaptoetanol (0.2% v/v) for 30 minutes at RT and then  
623 run in a denaturing second dimension electrophoresis (2D-SDS PAGE). The gels were run in  
624 MOPs buffer and then transferred to a nitrocellulose membrane. Immunodetection was performed  
625 as previously described. Primary antibodies used for immunoblotting of BN-PAGE are listed in  
626 Supplemental Dataset 4.  
627

### 628 ***Protein extraction, immunoblotting and immunoprecipitation***

629 To prepare total cell lysates for immunoblot analysis, cells were washed twice with cold Dulbecco's  
630 Phosphate-Buffered Saline (PBS; GIBCO, 14190169), scraped from the dishes and collected in  
631 tubes, then centrifuged at 16000g for 10 minutes at 4°C. For liver samples, tissue was pulverized  
632 or isolated mitochondria were spun at 3000g for 10 minutes at 4°C. Cell or mitochondria pellet or  
633 tissue powder were resuspended in RIPA buffer (Tris pH 7.4 50mM; NaCl 150 mM; Triton X-100  
634 (EuroMedex, 2000C) 1%; Sodium Deoxycholate 0.05% (Sigma-Aldrich, D6750); SDS 0.10%;  
635 EDTA 1 mM; protease inhibitors and PhosphoStop Inhibitors (Roche), homogenized with a pestle  
636 (Eppendorf, 033522) and incubated at 4°C for 30 minutes on a rotating wheel, then spun at  
637 16000g for 10 minutes. Protein concentration was determined with Bradford assay using a plate  
638 reader (TECAN). Protein extracts were prepared in Laemmli Buffer (Bio-Rad, 1610747) with 2-

639 Mercaptoethanol 355mM (Sigma-Aldrich, M3148) and boiled at 95°C for 5 minutes, then resolved  
640 by SDS-PAGE (Mini Protean chamber and TGX gels, Bio-Rad) and transferred onto nitrocellulose  
641 membrane (Trans-blot Turbo Transfer system and kit, Bio-Rad) followed by blocking with 3% milk  
642 for 30 minutes. Membranes were then incubated with the primary antibodies (listed in Table 2) and  
643 HRP-linked secondary antibodies (anti-mouse or anti-rabbit IgG; Thermo Fisher Scientific,  
644 10368172 and 11034). Clarity Western ECL (Bio-Rad) was used for the detection with ChemiDoc  
645 (Bio-Rad). Densitometric analysis of immunoblots was performed using Image Lab software (Bio-  
646 Rad). The signal of the quantified bands was normalized to loading controls or Stain-free TGX  
647 staining as indicated<sup>70</sup> and presented as fold difference over control treatment or control genotype  
648 as the invariant control.

649

## 650 ***Proteomics***

651 Liver extract proteins were extracted and denatured in RIPA buffer. Samples were sonicated using  
652 a Vibracell 75186 and a miniprobe 2 mm (Amp 80% // Pulse 10 off 0.8, 3 cycles) and further  
653 centrifuged. Protein assay was performed on supernatant (Pierce 660 nm, according to  
654 manufacturer instructions) and 100 µg of each extract was delipidated and cleaned using a  
655 Chloroform / Methanol / Water precipitation method. Briefly, 4 volume of ice-cold methanol were  
656 added to the sample and vortex, 2 volume of ice-cold chloroform were added and vortex and 3  
657 volume of ice-cold water was added and vortex. Samples were centrifuged 5 min at 5000 g. The  
658 upper layer was removed and proteins at the interface were kept. Tubes were filled with ice-cold  
659 methanol and centrifuged at max speed for 5 min. Resulting protein pellet was air-dried and then  
660 dissolved in 130 µl of 100mM NaOH before adding 170 µl of Tris 50 mM pH 8.0, tris (2-  
661 carboxyethyl)phosphine (TCEP) 5 mM and chloroacetamide (CAA) 20 mM. The mixture was  
662 heated 5 min at 95 °C and then cooled on ice. Endoprotease LysC (1µg) was use for an 8h  
663 digestion step at (37° C) followed with a trypsin digestion (1 µg) at 37°C for 4 h. Digestion was  
664 stopped adding 0.1% final of trifluoroacetic acid (TFA). Resulting peptides were desalted using a  
665 C18 stage tips strategy (Elution at 80% Acetonitrile (ACN) on Empore C18 discs stacked in a P200  
666 tips) and 30 µg of peptides were further fractionated in 4 fractions using  
667 poly(styrenedivinylbenzene) reverse phase sulfonate (SDB-RPS) stage-tips method as previously



668 described<sup>71,72</sup>. Four serial elutions were applied as following: elution 1 (80 mM Ammonium formate  
669 (AmF), 20% (v/v) ACN, 0.5% (v/v) formic acid (FA)), elution 2 (110 mM AmF, 35% (v/v) ACN, 0.5%  
670 (v/v) FA), elution 3 (150 mM AmmF, 50% (v/v) ACN, 0.5% (v/v) FA) and elution 4 (80% (v/v) ACN,  
671 5 % (v/v) ammonium hydroxide). All fractions were dried and resuspended in 0.1% FA before  
672 injection.

### 673 NanoLC-MS/MS

674 LC-MS/MS analysis of digested peptides was performed on an Orbitrap Q Exactive Plus mass  
675 spectrometer (Thermo Fisher Scientific, Bremen) coupled to an EASY-nLC 1200 (Thermo Fisher  
676 Scientific). A home-made column was used for peptide separation (C<sub>18</sub> 50 cm capillary column  
677 picotip silica emitter tip (75 µm diameter filled with 1.9 µm Reprosil-Pur Basic C<sub>18</sub>-HD resin, (Dr.  
678 Maisch GmbH, Ammerbuch-Entringen, Germany)). It was equilibrated and peptide were loaded in  
679 solvent A (0.1 % FA) at 900 bars. Peptides were separated at 250 nl.min<sup>-1</sup>. Peptides were eluted  
680 using a gradient of solvent B (ACN, 0.1 % FA) from 3% to 7% in 8 min, 7% to 23% in 95 min, 23%  
681 to 45% in 45 min (total length of the chromatographic run was 170 min including high ACN level  
682 step and column regeneration). Mass spectra were acquired in data-dependent acquisition mode  
683 with the XCalibur 2.2 software (Thermo Fisher Scientific, Bremen) with automatic switching  
684 between MS and MS/MS scans using a top 12 method. MS spectra were acquired at a resolution  
685 of 35000 (at *m/z* 400) with a target value of  $3 \times 10^6$  ions. The scan range was limited from 300 to  
686 1700 *m/z*. Peptide fragmentation was performed using higher-energy collision dissociation (HCD)  
687 with the energy set at 27 NCE. Intensity threshold for ions selection was set at  $1 \times 10^6$  ions with  
688 charge exclusion of  $z = 1$  and  $z > 7$ . The MS/MS spectra were acquired at a resolution of 17500 (at  
689 *m/z* 400). Isolation window was set at 1.6 Th. Dynamic exclusion was employed within 45 s.

### 690 Data Processing

691 Data were searched using MaxQuant (version 1.5.3.8) using the Andromeda search engine<sup>73</sup>  
692 against a reference proteome of *Mus musculus* (53449 entries, downloaded from Uniprot the 24<sup>th</sup> of  
693 July 2018). The following search parameters were applied: carbamidomethylation of cysteines was  
694 set as a fixed modification, oxidation of methionine and protein N-terminal acetylation were set as  
695 variable modifications. The mass tolerances in MS and MS/MS were set to 5 ppm and 20 ppm  
696 respectively. Maximum peptide charge was set to 7 and 5 amino acids were required as minimum

697 peptide length. A false discovery rate of 1% was set up for both protein and peptide levels. All 4  
698 fractions per sample were gathered and the iBAQ intensity was used to estimate the protein  
699 abundance within a sample<sup>74</sup>.

700 The label-free quantitative (LFQ) proteomics data was annotated in Perseus v.1.6.14.0<sup>75</sup> with  
701 Mouse MitoCarta 3.0<sup>77</sup> for individual OXPHOS complexes, mitoribosome and whole mitochondria  
702 using uniprot IDs. The Relative Complex Abundance (RCA) of the OXPHOS and mitoribosome  
703 were plotted with an in-house R script (R v.4.0.3, R studio v.1.3.1093) correcting for differential  
704 mitochondrial content using the ratio mean of LFQ values of mitochondria “+” annotations from  
705 MitoCarta 3.0. The mean of normalized values and standard deviation were calculated for each  
706 subunit of each complex comparing the LMKO and control mouse values from quantitative  
707 proteomics data along with the 95% confidence interval based on the t-statistic for each complex.  
708 A paired t-test calculated the significance between the LMKO and control mouse values for each  
709 complex. P-value \*\*\* =  $p \leq 0.001$ , ns= non-significant.

710 Mass spectrometry data have been deposited at the ProteomeXchange Consortium  
711 (<http://www.proteomexchange.org>) via the PRIDE partner repository<sup>76,77</sup> with the dataset identifier  
712 PXD041197.

713

#### 714 **Co-Immunoprecipitation assay**

715 500  $\mu$ g of cardiac liver mitochondria were freshly isolated from heart tissue of cardiomyocyte  
716 specific Flag-MTFP1 Knock-In (KI) mice (*Alb-Cre<sup>tg/+</sup>Mtfp1<sup>+/+</sup>*, *CAG<sup>tg/+</sup>*) and Control mice (*Albe-  
717 Cre<sup>+/+</sup>Mtfp1<sup>+/+</sup>*, *CAG<sup>tg/+</sup>*) as described above. Mitochondria were lysed in IP buffer (20 mM HEPES-  
718 KOH pH 7.5, 150 mM NaCl, 0.25% Triton X-100, protease inhibitor cocktail) on ice for 20 min and  
719 then centrifugated at 10000 g, 4°C for 15 min. Supernatant obtained by centrifugation was then  
720 incubated with 20  $\mu$ L of anti-FLAG magnetic beads (Sigma M8823) for 2 hours at 4°C. The  
721 immunocomplexes were then washed with IP buffer without Triton X-100 and eluted with Laemmli  
722 Sample Buffer 2x at 95°C for 5 min. Protein were stacked in a 15 % SDS-PAGE gel with a 10 min  
723 long migration at 80 V. Proteins were fixed in gel and migration was visualized using the Instant  
724 Blue stain (Expedeon). Bands were excised for digestion. Gel bands were washed twice in  
725 Ammonium bicarbonate (AmBi) 50 mM, once with AmBi 50 mM / ACN 50 % and once with 100%

726 ANC. Gel bands were incubated for 30 min at 56°C in 5 mM dithiothreitol (DTT) solution for  
727 reduction. Gel bands were washed in AmBi 50 mM and then in 100% ACN. Alkylation was  
728 performed at room temp in the dark by incubation of the gel bands in Iodocateamide 55 mM  
729 solution. Gel bands were washed twice in AmBi 50mM and in 100% ACN. 600 ng of trypsin were  
730 added for 8h digestion at 37°C. Peptides were extracted by collecting 3 washes of the gel bands  
731 using AmBi 50 mM / 50 % ACN and 5 % FA. Peptides clean up and desalting was done using  
732 Stage tips (2 disc Empore C18 discs stacked in a P200 tip).

733 LC-MS/SM analysis of digested peptides was performed on an Orbitrap Q Exactive HF mass  
734 spectrometer (Thermo Fisher Scientific, Bremen) coupled to an EASY-nLC 1200 (Thermo Fisher  
735 Scientific). A home-made column was used for peptide separation (C<sub>18</sub> 30 cm capillary column  
736 picotip silica emitter tip (75 µm diameter filled with 1.9 µm Reprosil-Pur Basic C<sub>18</sub>-HD resin, (Dr.  
737 Maisch GmbH, Ammerbuch-Entringen, Germany)). It was equilibrated and peptide were loaded in  
738 solvent A (0.1 % FA) at 900 bars. Peptides were separated at 250 nl.min<sup>-1</sup>. Peptides were eluted  
739 using a gradient of solvent B (ACN, 0.1 % FA) from 3% to 26% in 105 min, 26% to 48% in 20 min  
740 (total length of the chromatographic run was 145 min including high ACN level step and column  
741 regeneration). Mass spectra were acquired in data-dependent acquisition mode with the XCalibur  
742 2.2 software (Thermo Fisher Scientific, Bremen) with automatic switching between MS and MS/MS  
743 scans using a top 12 method. MS spectra were acquired at a resolution of 60000 (at *m/z* 400) with  
744 a target value of  $3 \times 10^6$  ions. The scan range was limited from 400 to 1700 *m/z*. Peptide  
745 fragmentation was performed using HCD with the energy set at 26 NCE. Intensity threshold for  
746 ions selection was set at  $1 \times 10^5$  ions with charge exclusion of  $z = 1$  and  $z > 7$ . The MS/MS spectra  
747 were acquired at a resolution of 15000 (at *m/z* 400). Isolation window was set at 1.6 Th. Dynamic  
748 exclusion was employed within 30 s. Data are available via ProteomeXchange with identifier  
749 PXD041197.

#### 750 Data Processing

751 Data were searched using MaxQuant (version 1.6.6.0) [1,2] using the Andromeda search engine  
752 [3] against a reference proteome of *Mus musculus* (53449 entries, downloaded from Uniprot the  
753 24<sup>th</sup> of July 2018). A modified sequence of the protein MTP18 with a Flag tag in its N-ter part was  
754 also searched.

755 The following search parameters were applied: carbamidomethylation of cysteines was set as a  
756 fixed modification, oxidation of methionine and protein N-terminal acetylation were set as variable  
757 modifications. The mass tolerances in MS and MS/MS were set to 5 ppm and 20 ppm respectively.  
758 Maximum peptide charge was set to 7 and 5 amino acids were required as minimum peptide  
759 length. A false discovery rate of 1% was set up for both protein and peptide levels. The iBAQ  
760 intensity was used to estimate the protein abundance within a sample.

761 Quantitative analysis was based on pairwise comparison of intensities. Values were log-  
762 transformed (log<sub>2</sub>). Reverse hits and potential contaminant were removed from the analysis.  
763 Proteins with at least 2 peptides (including one unique peptide) were kept for further statistics.  
764 Intensities values were normalized by median centering within conditions (normalizedD function of  
765 the R package DAPAR). Remaining proteins without any iBAQ value in one of both conditions  
766 have been considered as proteins quantitatively present in a condition and absent in the other.  
767 They have therefore been set aside and considered as differentially abundant proteins. Next,  
768 missing values were imputed using the impute.MLE function of the R package [imp4](#). Statistical  
769 testing was conducted using a limma t-test thanks to the R package limma<sup>113</sup>. An adaptive  
770 Benjamini-Hochberg procedure was applied on the resulting p-values thanks to the function  
771 `adjust.p` of R package `cp4p`<sup>114</sup> using the robust method previously described<sup>115</sup> to estimate the  
772 proportion of true null hypotheses among the set of statistical tests. The proteins associated to an  
773 adjusted p-value inferior to a FDR level of 1% have been considered as significantly differentially  
774 abundant proteins. Mass spectrometry data have been deposited at the ProteomeXchange  
775 Consortium (<http://www.proteomexchange.org>) via the PRIDE partner repository<sup>103,104</sup> with dataset  
776 identifier that is pending

777

### 778 **Liver RNA sequencing and RT-qPCR**

779 Total RNA was isolated from 50–100 mg of snap-frozen liver tissue by the NucleoSpin RNA kit  
780 (Macherey-Nagel, 740955). Quality control was performed on an Agilent BioAnalyzer. Libraries  
781 were built using a TruSeq Stranded mRNA library Preparation Kit (Illumina, USA) following the  
782 manufacturer's protocol. Two runs of RNA sequencing were performed for each library on an  
783 Illumina NextSeq 500 platform using paired-end 75bp. The RNA-seq analysis was performed with

784 Sequana. In particular, we used the RNA-seq pipeline (version 0.9.13)  
785 ([https://github.com/sequana/sequana\\_rnaseq](https://github.com/sequana/sequana_rnaseq)) built on top of Snakemake 5.8.1<sup>78</sup>. Reads were  
786 trimmed from adapters using Cutadapt 2.10 then mapped to the mouse reference genome  
787 GRCm38 using STAR 2.7.3a<sup>79</sup>. FeatureCounts 2.0.0 was used to produce the count matrix,  
788 assigning reads to features using annotation from Ensembl GRCm38\_92 with strand-specificity  
789 information<sup>80</sup>. Quality control statistics were summarized using MultiQC 1.8<sup>81</sup>. Statistical analysis  
790 on the count matrix was performed to identify differentially regulated genes, comparing different  
791 diets among same genotypes or different genotypes under same diet. Clustering of transcriptomic  
792 profiles were assessed using a Principal Component Analysis (PCA). Differential expression  
793 testing was conducted using DESeq2 library 1.24.0<sup>82</sup> scripts based on SARTools 1.7.0 indicating  
794 the significance (Benjamini-Hochberg adjusted p-values, false discovery rate FDR < 0.05) and the  
795 effect size (fold-change) for each comparison. Over-representation analysis (ORA) was performed  
796 to determine if genes modulated by HFD in control or LMKO mice are more present in specific  
797 pathways. ORA was performed on WebGestalt (<https://www.webgestalt.org/>). RNAseq data have  
798 been deposited at ENA with the dataset identifier E-MTAB-12920.  
799 For RT-qPCR, 1 µg of total RNA was converted into cDNA using the iScript Reverse Transcription  
800 Supermix (Bio-Rad). RT-qPCR was performed using the CFX384 Touch Real-Time PCR Detection  
801 System (Bio-Rad) and SYBR® Green Master Mix (Bio-Rad) using the primers listed in  
802 Supplemental Dataset 4. Gapdh was amplified as internal standard. Data were analyzed  
803 according to the 2<sup>-ΔΔCT</sup> method<sup>83</sup>.

#### 804 ***Primary hepatocyte isolation and imaging***

805 Primary hepatocytes were isolated from 6-8 week-old mice as previously described<sup>84</sup>.  
806 Briefly, a catheter (22G feeding needle) was connected to a pump and inserted into the vena cava.  
807 Livers were perfused first with perfusion buffer (NaCl 0.15M; Potassium Chloride (KCl, 2.7mM;  
808 EuroMedex; P017); Sodium phosphate dibasic (Na<sub>2</sub>HPO<sub>4</sub>, 0.2mM; Sigma-Aldrich 255793);  
809 HEPES-KOH pH 7.4 10mM and EDTA 0.5mM, pH 7.65) at the speed of 3.5 ml/min for 10 minutes,  
810 and then with the collagenase buffer (NaCl 0.15M, KCl 2.7mM, Na<sub>2</sub>HPO<sub>4</sub> 0.2mM, HEPES-KOH pH  
811 7.4 10mM, Calcium Chloride (CaCl<sub>2</sub>, 0.8mM; Sigma-Aldrich C3881) and Collagenase type I

812 500µg/ml (Thermo Fisher Scientific, 17018029). Liver lobes were collected in Washing Medium  
813 (William's medium (Thermo Fisher Scientific) supplemented with 10% Fetal Bovine Serum (FBS;  
814 GIBCO, 10270), a mix of penicillin (100U/ml) and streptomycin (100µg/ml) (Pen-Strep; Sigma-  
815 Aldrich, P4333) and amphotericin B (Fungizone, 250ng/ml; GIBCO, 15290018)) and passed  
816 through a cell strainer. Cells were centrifuged at 40g for 2 minutes, supernatant was removed and  
817 resuspended again with Washing Medium. This procedure was repeated 3 times. Finally,  
818 hepatocytes were counted with Trypan Blue using the Countless II FL Automated Cell counter  
819 (Invitrogen) and plated at  $1.2 \times 10^5$  cells/cm<sup>2</sup> in Culturing Medium (William's medium supplemented  
820 with 20% FBS, a mix of Insulin (1,7µM), Transferrin (68,75nM) and Selenium (38,73nM) (ITS;  
821 Sigma-Aldrich, I3146), dexamethasone (25nM; Sigma-Aldrich, D4902), penicillin (100U/ml) and  
822 streptomycin (100µg/ml) and Fungizone (250ng/ml) on pre-coated plates (collagen I (40µg/ml,  
823 Gibco) and glacial acetic acid 0.1% (Sigma-Aldrich, A6283); and incubated at 37°C then washed  
824 with PBS.

825 For cell death assays, primary hepatocytes were seeded in Cell Carrier Ultra 96-well plates  
826 (PerkinElmer, 6055302), treated with NucBlue Solution (Thermo Fisher) (diluted 1 drop in 10 ml)  
827 for 30 minutes, then, after 2 washes in PBS, cells were treated or not with hydrogen peroxide  
828 (H<sub>2</sub>O<sub>2</sub>, 1mM; Sigma-Aldrich, 95294) in the presence of Propidium Iodide (PI; Thermo Fisher,  
829 640922) (1:500).. Cells were immediately imaged with the Operetta CLS High-Content imaging  
830 system (PerkinElmer) at 37°C and 5% CO<sub>2</sub>. Images were taken every 2 hours for 10 hours with a  
831 20x water-immersion objective (1.0 NA). PI and NucBlue were excited with the 530-560nm and  
832 355-385nm LEDs respectively. Images were analyzed using Harmony 4.9 software (Perkin Elmer)  
833 using the analysis sequence in Supplemental Dataset 4.

834 Quantification of mitochondrial morphology: primary hepatocytes were isolated from  
835 mitoYFP+ mice and seeded in Cell Carrier Ultra 96-well plates, treated with 2µM NucBlue for 30  
836 minutes, then, after 2 washes in PBS. Cells were immediately imaged with the Operetta CLS High  
837 Content imaging system at 37°C and 5% CO<sub>2</sub>. Images were taken 16 hours post-plating with a 63x  
838 water-immersion objective (1.15 NA). MitoYFP and Hoechst were excited with the 460-490nm and  
839 355-385nm LEDs respectively. Images were analyzed using the PhenoLOGIC supervised machine  
840 learning pipeline in Harmony 4.9 software (Perkin Elmer) with the analysis sequence in Table 4.

841 The algorithm was used to identify the best properties able to segregate into “Short” or “Long”  
842 populations according to their mitochondrial network. 50 cells of each population were manually  
843 selected to for supervised machine learning training. Dead cells identified by propidium iodide were  
844 excluded directly by the algorithm and not included in the quantification. To mimic HFD steatosis in  
845 primary hepatocytes isolated, culture medium of the cells was supplemented with Intralipid (0.65%)  
846 for 24 hours. Intralipid is a complex lipid emulsion composed linoleic, oleic, palmitic, and stearic  
847 acids. BODIPY™ 558/568 C12 (Invitrogen D3835) was used to stain intracellular lipid  
848 accumulation.

849

### 850 **Statistical Analyses**

851 Experiments were repeated at least three times and quantitative analyses were conducted blindly.  
852 Randomization of groups (e.g., different genotypes) was performed when simultaneous, parallel  
853 measurements were not performed (e.g., Oroboros, hepatocyte isolation). For high-throughput  
854 measurements (e.g., mitochondrial morphology, cell death), all groups were measured in parallel  
855 to reduce experimental bias. Statistical analyses were performed using GraphPad Prism v9  
856 software. Data are presented as mean  $\pm$  SD or SEM where indicated. The statistical tests used,  
857 and value of experiment replicates are described in the figure legends. Comparisons between two  
858 groups were performed by unpaired two-tailed T test. To compare more than two groups or groups  
859 at multiple time points 1-way ANOVA or 2-way ANOVA was applied. Tests were considered  
860 significant at p-value  $< 0.05$  (\*p $< 0.05$ ; \*\*p $< 0.01$ ; \*\*\*p $< 0.001$ ; \*\*\*\*p $< 0.0001$ ).

861

862

863 **Figure legends**

864 **Figure 1. Hepatic deletion of *Mtfp1* in mice does not impair basal liver function.**

- 865 **A)** Generation of hepatocyte-specific *Mtfp1* knockout mice (LMKO). Conditional *Mtfp1*<sup>LoxP/LoxP</sup>  
866 mice were crossed to Alb-Cre recombinase mice to generate LMKO mice. *Mtfp1* exons 2 and  
867 3 are flanked by LoxP sites (blue arrowheads) and a single FRT site (green arrowhead), which  
868 are excised by Cre-recombinase to yield the deleted ( $\Delta$ ) *Mtfp1* allele.
- 869 **B)** PCR genotyping of *Mtfp1* alleles from DNA isolated from indicated different organs of a  
870 control and a LMKO mice allele-specific primers (Supplemental Dataset 4).
- 871 **C)** Normalized *Mtfp1* expression in liver in control and LMKO mice at 24-weeks measured by  
872 RNAseq (Supplemental Dataset 1). n=4. Data are means  $\pm$  SD, unpaired Student's t  
873 test. \*\*\*\*p<0.001.
- 874 **D)** MTFP1, VDAC1, TOMM40 and TIMM20 protein levels. Equal amounts of protein extracted  
875 from livers of control (n=4) and LMKO (n=4) mice at 8 weeks of age separated by SDS-PAGE  
876 and immunoblotted with indicated antibodies.
- 877 **E)** Genotype distribution from *Mtfp1*<sup>LoxP/LoxP</sup> *Alb-Cre*<sup>tg/+</sup> x *Mtfp1*<sup>LoxP/LoxP</sup> intercrosses were not  
878 different from expected Mendelian distributions using two-tailed binomial tests of live female  
879 (n=202; p>0.9999) and male (n=155; p=0.7481) mice.
- 880 **F)** (Top) Representative images of livers from control and LMKO mice fed at 24 weeks of  
881 age. Scale bar=1cm. (Bottom) Representative H&E staining n=4-5. Scale bar=100 $\mu$ m.
- 882 **G)** Liver mass of 24-week old control and LMKO mice fed a normal chow (NCD) n=9. Data  
883 are means  $\pm$  SD. unpaired Student's t test, ns=not significant
- 884 **H)** Alanine (ALAT; left) and Aspartate transaminase (ASAT; right) levels in plasma of control  
885 (n=3) and LMKO (n=3) mice. Data are means  $\pm$  SD. unpaired Student's t test, ns=not  
886 significant. \*: p<0.05.
- 887 **I)** Cholesterol (left) and triglycerides (TG, right) levels in plasma from G). Data are means  $\pm$   
888 SD. unpaired Student's t test, ns=not significant.
- 889 **J)** Metabolic cage analyses of NCD-fed control and LMKO mice at 24 weeks of age. Total  
890 distance covered, food, and water during dark and light phases n=3. Data  
891 are means  $\pm$  SD. unpaired Student's t test, \*\*: p<0.01. ns=not significant



892

893 **Figure 2. *Mtfp1* deletion promotes mitochondrial respiration via OXPHOS upregulation**

894 **A)** Substrates from fatty acid oxidation (mustard) and glycolysis (purple, blue) are metabolized in  
895 the TCA cycle which delivers fuels the electron transport chain (ETC) complexes by providing  
896 NADH and FADH to complexes I (purple) and II (blue), respectively. ETC creates  
897 an electrochemical gradient driving the phosphorylation of ADP by Complex V. Specific inhibitors  
898 of complex I (rotenone), complex V (oligomycin).

899 **B)** Oxygen flux ( $JO_2$ ) of isolated liver mitochondria from 16-week old control and LMKO mice  
900 on NCD measured in the presence of pyruvate, glutamate, and malate (state 2) or succinate  
901 and rotenone (state 2) or palmitoyl carnitine and malate (state 2) followed by ADP (state 3).  
902 Non-phosphorylating respiration was measured in the presence of oligomycin (state 4).

903 Respiratory Control Ratio (State3:4) data are represented as the means  $\pm$  SD of 4 independent  
904 experiments. 2-tailed, unpaired Student's t test. \*:  $p < 0.05$ .

905 **C)** Respiratory Control Ratio (RCR) from 16 week old control and LMKO mice on NCD measured  
906 in the presence of pyruvate, glutamate and malate plus ADP (state 3) or palmitoyl carnitine and  
907 malate plus ADP (state 3) divided Non-phosphorylating respiration in the presence of oligomycin  
908 (state 4).

909 **D)** Mitochondrial membrane potential ( $\Delta\Psi$ ) measured by quenching of Rhodamine 123  
910 (RH123) fluorescence in liver mitochondria from B).  $\Delta\Psi$  was measured in presence of  
911 pyruvate, malate, and glutamate (PGM) (state 2) followed by the addition of ADP (state 3)  
912 and Oligomycin (OLGM, state 4), CCCP and potassium cyanide (KCN). Data represent  
913 mean  $\pm$  SD; Multiple t-test.

914 **E)** Complex IV activity assessed in isolated liver mitochondria from NCD-fed 16-week old  
915 control and LMKO mice by recording oxygen flux ( $JO_2$ ) in the presence of Antimycin A  
916 (AMA), Ascorbate and N,N,N',N'-Tetramethyl-p-phenylenediamine dihydrochloride (TMPD),  
917 previously incubated with of pyruvate, glutamate, and malate (PGM) and ADP.  $n=5$ . Data are  
918 means  $\pm$  SD. 2-tailed, unpaired Student's t test. \*:  $p < 0.05$ .

919 **F)** Complex V (ATP synthase) activity assessed in isolated liver mitochondria from NCD-fed  
920 16-week old control and LMKO mice in the reverse mode in the presence of ATP. Oligomycin

921 (OLGM) or ADP were used as negative controls. n=10. Data are means  $\pm$  SD. 2-tailed,  
922 unpaired Student's t test. \*: p<0.05.

923 **G)** Mitoplast respiration assessment. Mitoplasts were supplied with either NADH, malate, and ADP  
924 (complex I) or FADH, rotenone, and ADP (complex II) n=5. Data are means  $\pm$  SD. 2-tailed,  
925 unpaired Student's t test. \*: p<0.05.

926 **H)** (Top) Volcano plot of liver proteome of LMKO mice analyzed by mass spectrometry. (Purple)  
927 Mitochondrial proteins (MitoCarta 3.0), (Green) Non-mitochondrial proteins more abundant in  
928 control liver. (Blue) Non-mitochondrial proteins significantly more abundant in LMKO liver.  
929 (Bottom) Relative complex abundance (RCA) plot comparing the levels of the OXPHOS  
930 complexes (CI-CV) and the mitoribosome (mtribo) between LMKO and control mice fed. NCD.  
931 The graph represents the relative values of each complex ratio between LMKO and controls.  
932 The dotted line represents the control mean value of each complex and error bars represent  
933 95% confidence interval of the mean. Paired t-test. \*\*\* = p<0.001, ns=non-significant.

934 **I)** Proteins levels of different OXPHOS complexes subunits. Equal amounts of protein  
935 extracted from hepatic mitochondria isolated from NCD-fed 16-week old control (n=4) and  
936 LMKO (n=4) mice were separated by SDS-PAGE, immunoblotted with indicated antibodies  
937 (left) and quantified by densitometry (right) relative to Timm22 loading control. Data are means  
938  $\pm$  SD. 2-tailed, unpaired Student's t test. \*: p<0.05.

939 **J)** 1D BN-PAGE (left) and densitometric quantification (right) of OXPHOS complexes in hepatic  
940 mitochondria isolated from NCD-fed 16-weeks old control and LMKO. n=4. Data are means  $\pm$  SD.  
941 2-tailed, unpaired Student's t test. \*: p<0.05.

942

943 **Figure 3. MTFP1 interacts with various IMM components in the liver.**

944 **A)** Generation of transgenic (Tg) Hepatocyte<sup>FLAG-MTFP1</sup> mice constitutively expressing FLAG-MTFP1  
945 from the *Ros26* locus.

946 **B)** Protease protection assay of liver mitochondria isolated from control and transgenic (Tg)  
947 Hepatocyte<sup>FLAG-MTFP1</sup> mice analyzed by immunoblot with indicated antibodies.

948 **C)** Liver mitochondria co-immunoprecipitation (co-IP) in WT and FALG\_MTFP1 mitochondria.  
949 Elution fraction (Elu).

950 **D)** Volcano plot of the FLAG-MTFP1 interactome analyzed by mass spectrometry (left). (Purple)  
951 Mitochondrial proteins exclusively present in FLAG-MTFP1 eluates (binary interactors) or enriched  
952 greater than two-fold listed in Supplementary Data 5. (Green) Non-mitochondrial proteins enriched  
953 in Hepatocyte<sup>FLAG-MTFP1</sup> livers. (Blue) Non-mitochondrial proteins enriched in control liver. (Right)  
954 Functional classification of 113 mitochondrial proteins identified in Co-IP eluates (Supplementary  
955 Data 4).

956 **E)** Second dimension electrophoresis (2D BN-PAGE) analysis of hepatic mitochondria isolated  
957 from control (top) and cMKO (bottom) mice fed a NCD immunoblotted using the indicated  
958 antibodies.

959

960 **Figure 4. Hepatic deletion of *Mtfp1* protects mice from high fat diet-induced steatosis.**

961 **A)** Representative images of livers from control and LMKO mice fed a normal chow diet  
962 (NCD, from Fig. 1D) or a high fat diet (HFD) for 16 weeks.

963 **B)** Liver weight of 24-week old control and LMKO mice fed a NCD or HFD for 16 weeks. n=7. Data  
964 are means ± SD. 2-way ANOVA, \*: p<0.05, \*\*: p<0.01, \*\*\*: p<0.001, \*\*\*\*: p<0.0001

965 **C)** Body mass of control and LMKO mice fed a NCD or HFD for 16 weeks. n=7. Data are  
966 means ± SD. 2-way ANOVA, \*: p<0.05, \*\*: p<0.01, \*\*\*: p<0.001, \*\*\*\*: p<0.0001.

967 **D)** Triglycerides (TG) measurement in liver tissue from 24-week old control and LMKO mice  
968 fed a NCD or HFD for 16 weeks. n=4-5. Data are means ± SD. 2-way ANOVA, \*\*: p<0.01,

969 **E)** H&E staining of control and LMKO livers from A). Scale bar=100µm.

970 **F)** Alanine (ALAT; left) and Aspartate transaminase (ASAT; right) levels in plasma of 24-  
971 week old control and LMKO mice fed a NCD or HFD for 16 weeks. Data are means ± SD. 2-  
972 way ANOVA, \*: p<0.05, \*\*\*: p<0.001, \*\*\*\*: p<0.0001

973 **G)** Differential modulation of liver gene expression by HFD. Upregulation (left) and  
974 downregulation (right) of mitochondrial (pink) and non-mitochondrial genes (orange or teal) in  
975 LMKO and control livers.

976 **H)** Pathway enrichment analysis of differentially expressed genes depicted in G).

977 **I)** TUNEL staining of control and LMKO livers from A). Scale bar=100µm

978

979 **Figure 5. LMKO mice are protected against diet-induced metabolic dysregulation**

980 **A)** Whole-body Respiratory Exchange ratios (RER;  $VCO_2/VO_2$ ) in control and LMKO

981 mice after 16 weeks of HFD. n=3. Data are means  $\pm$  SD. 2-way ANOVA, \*\*:  $p < 0.01$ .

982 **B)** Pyruvate Tolerance Test performed after 18h fasting. Left panel: glycaemia measured at

983 indicated time. Right panel: area under the curve (AUC). n=4 NCD; n=5 HFD groups. Data are

984 means  $\pm$  SD. 2-way ANOVA, \*:  $p < 0.05$ , \*\*:  $p < 0.01$ , \*\*\*\*:  $p < 0.0001$ .

985 **C)** Glucose Tolerance Test performed after 18h fasting. Left panel: glycaemia measured at

986 indicated time. Right panel: area under the curve (AUC). n=4-9. Data are means  $\pm$  SD 2-way

987 ANOVA, \*\*:  $p < 0.01$ .

988 **D)** Insulin Tolerance Test performed after 6 hours fasting. Left panel: glycaemia measured at

989 indicated time after insulin injection. Right panel: area under the curve (AUC). n=4. Data are

990 means  $\pm$  SD. 2-way ANOVA, \*:  $p < 0.05$ , \*\*:  $p < 0.01$ , \*\*\*:  $p < 0.0001$ , \*\*\*\*:  $p < 0.0001$ .

991 **E)** Body composition analysis of control and LMKO mice fed NCD or HFD by Nuclear

992 Magnetic Resonance (NMR). n=5. Left panel: fat mass; right panel: lean mass. Data are

993 means  $\pm$  SD. 2-way ANOVA, \*:  $p < 0.05$ , \*\*:  $p < 0.01$ , \*\*\*:  $p < 0.0001$ , ns=not significant

994 **F)** Plasma cholesterol (left) and triglycerides (TG) in control and LMKO mice fed NCD or

995 HFD. n=4-5. Data are means  $\pm$  SD. 2-way ANOVA, \*:  $p < 0.05$ , \*\*:  $p < 0.01$ , \*\*\*:  $p < 0.0001$ , ns=not

996 significant

997 **G)** Epididymal white adipose tissue (eWAT) mass in control and LMKO mice fed NCD or

998 HFD. n=5 NCD, n=7 HFD. Data are means  $\pm$  SD. 2-way ANOVA, \*:  $p < 0.05$ , \*\*:  $p < 0.01$ .

999 **H)** Ex vivo steatosis measurement. Representative images of primary hepatocytes isolated

1000 from control and LMKO mice treated with IntraLipid (0.65%) for 24h and stained for

1001 nuclei (NucBlue, blue) and lipid droplets (BODIPY, orange).

1002 **I)** BODIPY intensity quantification of H) Data are means of 3 independent experiments  $\pm$  SD.

1003 unpaired Student's t test, \*\*:  $p < 0.01$

1004

1005 **Figure 6. Hepatic deletion of *Mtfp1* protects mice from FAS-induced liver damage.**

1006 **A)** Representative images of livers from control (n=2) and LMKO (n=4) mice treated with

1007 FAS or NaCl for 24 hours.

1008 **B)** Alanine (ALAT; left) and Aspartate transaminase (ASAT; right) levels in plasma of mice  
1009 from A). Data are means  $\pm$  SD. unpaired Student's t test, \*:  $p < 0.05$ , \*\*:  $p < 0.01$ .  
1010 **C)** H&E staining of control and LMKO livers from A). Scale bar=100 $\mu$ m.  
1011 **D)** TUNEL staining of control and LMKO livers from A). Scale bar=100 $\mu$ m.  
1012 **E)** Representative of high content imaging of primary hepatocytes from control and LMKO mice  
1013 treated with or without H<sub>2</sub>O<sub>2</sub> at 4 hours (1mM) treatment. Blue: nuclei; Orange: propidium iodide  
1014 (PI).  
1015 **F)** Cell death quantification of PI uptake of 3 independent experiments from E). Data are means  $\pm$   
1016 SEM. 2-way ANOVA, \*:  $p < 0.05$ .  
1017 **G)** Mitochondrial permeability transition pore (mPTP) opening assay. Liver mitochondria  
1018 from control and LMKO mice were treated with CaCl<sub>2</sub> 120 $\mu$ M to induce the mPTP opening  
1019 by light scattering at 540nm. Cyclosporin A (CsA) 1  $\mu$ M used to block mPTP opening. Data  
1020 are means of 3 independent experiments  $\pm$  SEM. 2-way ANOVA, \*:  $p < 0.05$ .

1021

## 1022 **Figure 7. Model for the regulation of liver resilience by MTFP1**

1023 *Mtfp1* deletion in hepatocytes of liver-specific *Mtfp1* knockout (LMKO) mice promotes liver  
1024 resilience in vivo by 1) increasing the resistance to mitochondrial permeability transition pore  
1025 (mPTP) opening and liver apoptosis and 2) enhancing oxidative phosphorylation (OXPHOS)  
1026 activity and resistance against fatty liver disease (hepatic steatosis) induced by chronic high fat  
1027 diet (HFD) feeding.

1028

## 1029 **Supplemental Figures**

### 1030 **Figure S1. Generation and characterization of *Mtfp1* hepatocyte-specific knockout mice**

1031 **A)** Targeting strategy for conditional inactivation of mouse *Mtfp1* in LMKO mice. To allow deletion  
1032 of *Mtfp1* exons 2 and 3 were flanked in both cases by LoxP sites (blue arrowheads). Flox denotes  
1033 NeoR cassette containing LoxP targeted locus. LoxP denotes NeoR cassette-deleted targeted  
1034 locus.  $\Delta$  denotes deletion induced by Cre-recombinase. FRT sites (green) initially flank NeoR  
1035 cassette (yellow). Exons 2 and 3 were deleted by Cre-recombinase.

1036 **B)** Genotyping PCR for the distal LoxP site in the conditional *Mtfp1* locus from genomic DNA.

1037 The wild type (WT; 387 bp) and the conditional (LoxP; 469 bp) alleles are shown for *Mtfp*<sup>WT/WT</sup>,  
1038 *Mtfp*<sup>LoxP/WT</sup>, and *Mtfp*<sup>LoxP/LoxP</sup> mice.

1039 **C)** Respiratory Exchange Ratio (RER) for control and LMKO mice on fed a normal chow diet (NCD).  
1040 RER analyses for 24 hours are shown. Mean values for day and night periods. N=4. Data are means  
1041 ± SD. 2-tailed, unpaired Student's t test. ns=not significant.

1042 **D)** Upregulated (orange) and downregulated (cyan) genes in LMKO mice on a normal chow diet  
1043 corresponding to Supplemental Dataset 1.

1044

### 1045 **Figure S2. Impact of *Mtfp1* deletion on mitochondrial mass**

1046 **A)** Representative images of primary hepatocytes isolated from control and LMKO mice  
1047 expressing mitoYFP (green). Nuclei in blue. Scale bar=100µm.

1048 **B)** Quantification of mitochondrial imaging in primary hepatocytes from control and LMKO  
1049 expressing mitoYFP mice. Single cell mitoYFP intensity is normalized to hepatocyte area.

1050 **C)** Quantification of mitochondrial morphology in primary hepatocytes from control and LMKO mice  
1051 performed by supervised machine learning.

1052 **D)** Mitochondrial DNA content measured by qPCR relative to nuclear DNA in liver biopsies from  
1053 control and LMKO mice fed a normal chow (NCD) or high-fat (HFD) diets for 16 weeks. N=4. Data  
1054 are means ± SD. 2-way ANOVA, \*: p<0.05. \*\*: p<0.01.

1055 **E)** Mitochondrial surface determined by transmission electron microscopy (TEM) of control  
1056 and LMKO liver sections. Median (yellow dotted line) and Quartiles (solid colored line). 2-  
1057 tailed, unpaired Student's t test. ns=not significant.

1058

### 1059 **Figure S3. Diet-induced transcriptional remodeling in control and LMKO mice**

1060 **A)** Venn diagram overlap of upregulated genes in LMKO and control mice on normal chow diet  
1061 (NCD) or high fat diet (HFD) corresponding to Supplemental Dataset 1.

1062 **A)** Venn diagram overlap of downregulated genes in LMKO and control mice on normal chow diet  
1063 (NCD) or high fat diet (HFD) corresponding to Supplemental Dataset 1.

1064

### 1065 **Figure S4. Diet-induced proteomic remodeling in control and LMKO mice**

1066 **A)** (Top) Volcano plot of liver proteome of LMKO mice analyzed by mass spectrometry. (Purple)  
1067 Mitochondrial proteins (MitoCarta 3.0), (Green) Enriched non-mitochondrial proteins more  
1068 (Blue) Enriched non-mitochondrial proteins corresponding to Supplemental Dataset 3.  
1069 **B)** Relative complex abundance (RCA) plot comparing the levels of the OXPHOS  
1070 complexes (CI-CV) and the mitoribosome (mtribo). The graph represents the relative values  
1071 of each complex ratio between two groups. The dotted line represents the control mean value  
1072 of each complex and error bars represent 95% confidence interval of the mean. Paired t-test.  
1073 \*\*\* =  $p < 0.001$ , ns= non-significant.

1074

1075 **Figure S5. LMKO mice are protected against diet-induced metabolic dysregulation**

1076 **A)** Total food consumption during dark and light phases in HFD-fed control and LMKO mice.  
1077  $n=3$ . Data are means  $\pm$  SD. unpaired Student's t test, ns=not significant.

1078 **B)** Total water consumption during dark and light phases in HFD-fed control and  
1079 LMKO mice  $n=3$ . Data are means  $\pm$  SD. unpaired Student's t test, ns=not significant.

1080 **C)** Total distance covered during dark and light phases in HFD-fed control and LMKO mice.  
1081  $n=3$ . Data are means  $\pm$  SD. unpaired Student's t test, ns=not significant

1082 **D)** Plasma insulin levels measured in control and LMKO mice treated fed with NCD or  
1083 HFD after 16 hours fasting (0 minute) or fasting followed by glucose injection (30 minutes).  
1084  $n=4-5$ . Data are means  $\pm$  SD. 2-way ANOVA, \*\*\*:  $p < 0.001$

1085 **E)** Representative images of extrahepatic white adipose tissue (eWAT) after H&E staining  
1086 from control and LMKO mice fed with NCD or HFD for 16 weeks.  $n=4-5$ . Scale bar=100 $\mu$ m.

1087 **F)** Quantification of adipocyte area in G).Data are means  $\pm$  SD. 2-way ANOVA, \*:  $p < 0.05$ .

1088 **G)** Body weight of control and LMKO mice on NCD and HFD. Data are means  $\pm$  SD

1089 **H)** Fasting glycaemia of control and LMKO mice on NCD and HFD. Data are means  $\pm$  SD

1090

1091 **Figure S6. Hepatic deletion of *Mtfp1* protects mice from FAS-induced liver damage.**

1092 **A)** Lactate dehydrogenase (LDH) plasma levels of 16-week old control and LMKO after  
1093 treatment with FAS ( $n=4$ ) or NaCl ( $n=2$ ) for 24 hours. Data are means  $\pm$  SD. 2-tailed, unpaired  
1094 Student's t test. \*:  $p < 0.05$

1095 **B)** Liver to body weight ratio of 16-week old control and LMKO before and after treatment with  
1096 FAS (n=6) or NaCl (n=4) for 24 hours. Data are means  $\pm$  SD. 2-way ANOVA, \*: p<0.05 ns=not  
1097 significant.

1098

1099 **Figure S7. Differential MTFP1 expression in animal models and human patients**

1100 **A)** Venn diagram comparison of differentially expressed genes in MTFP1-deficient livers and  
1101 hearts from LMKO and cMKO mice. LMKO data are reported in Supplemental Dataset 1 and  
1102 cMKO data were reported previously<sup>15</sup>.

1103 **B)** Venn diagram comparison of differentially expressed proteins in MTFP1-deficient livers and  
1104 hearts from LMKO and cMKO mice. LMKO data are reported in Supplemental Dataset 2 and  
1105 cMKO data were reported previously<sup>15</sup>.

1106 **C)** Violin plot of *MTFP1* expression (transcripts per kilobase (TPkB) in NASH human patients  
1107 biopsies (GSE162694) previously analyzed<sup>67</sup>. F0-F4 scale refers to the severity of the severity of  
1108 fibrosis as previously described<sup>85</sup>. Data are means  $\pm$  SD. 1-way ANOVA, \*\*: p<0.01 \*\*\*\*: p<0.0001.

1109

1110

1111

1112

1113

1114



1115 **References**

- 1116 1. Samuel, V. T. & Shulman, G. I. Nonalcoholic Fatty Liver Disease as a Nexus of Metabolic and  
1117 Hepatic Diseases. *Cell Metab.* **27**, 22–41 (2018).
- 1118 2. Ye, Q. *et al.* Global prevalence, incidence, and outcomes of non-obese or lean non-alcoholic  
1119 fatty liver disease: a systematic review and meta-analysis. *Lancet Gastroenterol Hepatol* **5**,  
1120 739–752 (2020).
- 1121 3. Tilg, H. & Moschen, A. R. Evolution of inflammation in nonalcoholic fatty liver disease: the  
1122 multiple parallel hits hypothesis. *Hepatology* **52**, 1836–1846 (2010).
- 1123 4. Fromenty, B. & Roden, M. Mitochondrial alterations in fatty liver diseases. *J. Hepatol.* **78**, 415–  
1124 429 (2023).
- 1125 5. Giacomello, M., Pyakurel, A., Glytsou, C. & Scorrano, L. The cell biology of mitochondrial  
1126 membrane dynamics. *Nat. Rev. Mol. Cell Biol.* **21**, 204–224 (2020).
- 1127 6. Riley, J. S. & Tait, S. W. Mitochondrial DNA in inflammation and immunity. *EMBO Rep.* **21**,  
1128 e49799 (2020).
- 1129 7. Nassir, F. & Ibdah, J. A. Role of mitochondria in nonalcoholic fatty liver disease. *Int. J. Mol.*  
1130 *Sci.* **15**, 8713–8742 (2014).
- 1131 8. García-Ruiz, I. *et al.* High-fat diet decreases activity of the oxidative phosphorylation  
1132 complexes and causes nonalcoholic steatohepatitis in mice. *Dis. Model. Mech.* **7**, 1287–1296  
1133 (2014).
- 1134 9. Gorman, G. S. *et al.* Mitochondrial diseases. *Nat Rev Dis Primers* **2**, 16080 (2016).
- 1135 10. Koliaki, C. *et al.* Adaptation of hepatic mitochondrial function in humans with non-alcoholic  
1136 fatty liver is lost in steatohepatitis. *Cell Metab.* **21**, 739–746 (2015).
- 1137 11. Sanyal, A. J. *et al.* Nonalcoholic steatohepatitis: Association of insulin resistance and  
1138 mitochondrial abnormalities. *Gastroenterology* **120**, 1183–1192 (2001).
- 1139 12. Perry, R. J., Zhang, D., Zhang, X.-M., Boyer, J. L. & Shulman, G. I. Controlled-release  
1140 mitochondrial protonophore reverses diabetes and steatohepatitis in rats. *Science* **347**, 1253–  
1141 1256 (2015).

- 1142 13. Goedeke, L. *et al.* Controlled-release mitochondrial protonophore (CRMP) reverses  
1143 dyslipidemia and hepatic steatosis in dysmetabolic nonhuman primates. *Sci. Transl. Med.* **11**,  
1144 (2019).
- 1145 14. Parascandola, J. Dinitrophenol and bioenergetics: an historical perspective. *Mol. Cell.*  
1146 *Biochem.* **5**, 69–77 (1974).
- 1147 15. Donnarumma, E. *et al.* Mitochondrial Fission Process 1 controls inner membrane integrity and  
1148 protects against heart failure. *Nat. Commun.* **13**, 6634 (2022).
- 1149 16. Tondera, D. The mitochondrial protein MTP18 contributes to mitochondrial fission in  
1150 mammalian cells. *J Cell Sci* **118**, 3049–3059 (2005).
- 1151 17. Morita, M. *et al.* mTOR Controls Mitochondrial Dynamics and Cell Survival via MTFP1. *Mol.*  
1152 *Cell* **67**, 922-935.e5 (2017).
- 1153 18. Zhang, Y. *et al.* MTP18 overexpression contributes to tumor growth and metastasis and  
1154 associates with poor survival in hepatocellular carcinoma. *Cell Death Dis.* **9**, 956 (2018).
- 1155 19. Tondera, D. *et al.* Knockdown of MTP18, a novel phosphatidylinositol 3-kinase-dependent  
1156 protein, affects mitochondrial morphology and induces apoptosis. *J. Biol. Chem.* **279**, 31544–  
1157 31555 (2004).
- 1158 20. Duroux-Richard, I. *et al.* miR-125b controls monocyte adaptation to inflammation through  
1159 mitochondrial metabolism and dynamics. *Blood* **128**, 3125–3136 (2016).
- 1160 21. Ryaboshapkina, M. & Hammar, M. Human hepatic gene expression signature of non-alcoholic  
1161 fatty liver disease progression, a meta-analysis. *Sci. Rep.* **7**, 12361 (2017).
- 1162 22. Donnarumma, E. *et al.* Mitochondrial fission process 1 (MTFP1) controls bioenergetic  
1163 efficiency and prevents inflammatory cardiomyopathy and heart failure in mice. *bioRxiv*  
1164 2021.10.21.465262 (2021) doi:10.1101/2021.10.21.465262.
- 1165 23. Cretin, E. *et al.* High-throughput screening identifies suppressors of mitochondrial  
1166 fragmentation in OPA1 fibroblasts. *EMBO Mol. Med.* **13**, e13579 (2021).
- 1167 24. Rath, S. *et al.* MitoCarta3.0: an updated mitochondrial proteome now with sub-organelle  
1168 localization and pathway annotations. *Nucleic Acids Res.* **49**, D1541–D1547 (2021).
- 1169 25. Soltis, A. R. *et al.* Hepatic Dysfunction Caused by Consumption of a High-Fat Diet. *Cell Rep.*  
1170 **21**, 3317–3328 (2017).

- 1171 26. Commerford, S. R. *et al.* Diets enriched in sucrose or fat increase gluconeogenesis and G-6-  
1172 Pase but not basal glucose production in rats. *American Journal of Physiology-Endocrinology*  
1173 *and Metabolism* **283**, E545–E555 (2002).
- 1174 27. Lemonnier, D. Effect of age, sex, and site on the cellularity of the adipose tissue in mice and  
1175 rats rendered obese by a high-fat diet. *J Clin Invest* **51**, 2907–2915 (1972).
- 1176 28. Aung, L. H. H., Li, R., Prabhakar, B. S., Maker, A. V. & Li, P. Mitochondrial protein 18 (MTP18)  
1177 plays a pro-apoptotic role in chemotherapy-induced gastric cancer cell apoptosis. *Oncotarget*  
1178 **8**, 56582–56597 (2017).
- 1179 29. Varanita, T. *et al.* The OPA1-dependent mitochondrial cristae remodeling pathway controls  
1180 atrophic, apoptotic, and ischemic tissue damage. *Cell Metab.* **21**, 834–844 (2015).
- 1181 30. Elmore, S. A. *et al.* Recommendations from the INHAND Apoptosis/Necrosis Working Group.  
1182 *Toxicol Pathol* **44**, 173–188 (2016).
- 1183 31. Baines, C. P. *et al.* Loss of cyclophilin D reveals a critical role for mitochondrial permeability  
1184 transition in cell death. *Nature* **434**, 658–662 (2005).
- 1185 32. Karch, J. *et al.* Inhibition of mitochondrial permeability transition by deletion of the ANT family  
1186 and CypD. *Sci Adv* **5**, eaaw4597 (2019).
- 1187 33. Sebastián, D. *et al.* Mitofusin 2 (Mfn2) links mitochondrial and endoplasmic reticulum function  
1188 with insulin signaling and is essential for normal glucose homeostasis. *Proc. Natl. Acad. Sci.*  
1189 *U. S. A.* **109**, 5523–5528 (2012).
- 1190 34. Huang, Q. *et al.* TFAM loss induces nuclear actin assembly upon mDia2 malonylation to  
1191 promote liver cancer metastasis. *EMBO J.* **41**, e110324 (2022).
- 1192 35. Yamada, T. *et al.* Prevention and regression of megamitochondria and steatosis by blocking  
1193 mitochondrial fusion in the liver. *iScience* **25**, 103996 (2022).
- 1194 36. Cho, J. *et al.* Mitochondrial ATP transporter depletion protects mice against liver steatosis and  
1195 insulin resistance. *Nat. Commun.* **8**, 14477 (2017).
- 1196 37. Lesner, N. P. *et al.* Differential requirements for mitochondrial electron transport chain  
1197 components in the adult murine liver. *Elife* **11**, (2022).
- 1198 38. Aung, L. H. H. *et al.* Mitochondrial protein 18 is a positive apoptotic regulator in  
1199 cardiomyocytes under oxidative stress. *Clin. Sci.* **133**, 1067–1084 (2019).

- 1200 39. Yakar, S. *et al.* Normal growth and development in the absence of hepatic insulin-like growth  
1201 factor I. *PNAS* **96**, 7324–7329 (1999).
- 1202 40. Hill, B. G. *et al.* Integration of cellular bioenergetics with mitochondrial quality control and  
1203 autophagy. *Biol. Chem.* **393**, 1485–1512 (2012).
- 1204 41. Moyes, C. D., Mathieu-Costello, O. A., Brill, R. W. & Hochachka, P. W. Mitochondrial  
1205 metabolism of cardiac and skeletal muscles from a fast (*Katsuwonus pelamis*) and a slow  
1206 (*Cyprinus carpio*) fish. *Can. J. Zool.* **70**, 1246–1253 (1992).
- 1207 42. Suarez, R. K. Oxygen and the upper limits to animal design and performance. *J. Exp. Biol.*  
1208 **201**, 1065–1072 (1998).
- 1209 43. Srere, P. A. Organization of proteins within the mitochondrion. *Organized multienzyme*  
1210 *systems. Catalytic properties* 1–61 (1985).
- 1211 44. Forner, F., Foster, L. J., Campanaro, S., Valle, G. & Mann, M. Quantitative proteomic  
1212 comparison of rat mitochondria from muscle, heart, and liver. *Mol. Cell. Proteomics* **5**, 608–  
1213 619 (2006).
- 1214 45. Kim, T.-Y. *et al.* Metabolic labeling reveals proteome dynamics of mouse mitochondria. *Mol.*  
1215 *Cell. Proteomics* **11**, 1586–1594 (2012).
- 1216 46. Gross, N. J. Control of mitochondrial turnover under the influence of thyroid hormone. *J. Cell*  
1217 *Biol.* **48**, 29–40 (1971).
- 1218 47. Jakovcic, S., Swift, H. H., Gross, N. J. & Rabinowitz, M. Biochemical and stereological  
1219 analysis of rat liver mitochondria in different thyroid states. *J. Cell Biol.* **77**, 887–901 (1978).
- 1220 48. Arruda, A. P. *et al.* Chronic enrichment of hepatic endoplasmic reticulum-mitochondria contact  
1221 leads to mitochondrial dysfunction in obesity. *Nat. Med.* **20**, 1427–1435 (2014).
- 1222 49. Chouchani, E. T. *et al.* Complex I deficiency due to selective loss of Ndufs4 in the mouse  
1223 heart results in severe hypertrophic cardiomyopathy. *PLoS One* **9**, e94157 (2014).
- 1224 50. Wai, T. *et al.* Imbalanced OPA1 processing and mitochondrial fragmentation cause heart  
1225 failure in mice. *Science* **350**, aad0116 (2015).
- 1226 51. Piquereau, J. *et al.* Down-regulation of OPA1 alters mouse mitochondrial morphology, PTP  
1227 function, and cardiac adaptation to pressure overload. *Cardiovasc. Res.* **94**, 408–417 (2012).

- 1228 52. Song, M., Mihara, K., Chen, Y., Scorrano, L. & Dorn, G. W., 2nd. Mitochondrial fission and  
1229 fusion factors reciprocally orchestrate mitophagic culling in mouse hearts and cultured  
1230 fibroblasts. *Cell Metab.* **21**, 273–286 (2015).
- 1231 53. Graham, B. H. *et al.* A mouse model for mitochondrial myopathy and cardiomyopathy resulting  
1232 from a deficiency in the heart/muscle isoform of the adenine nucleotide translocator. *Nat.*  
1233 *Genet.* **16**, 226–234 (1997).
- 1234 54. Anderson, C. J. *et al.* ALS/FTD mutant CHCHD10 mice reveal a tissue-specific toxic gain-of-  
1235 function and mitochondrial stress response. *Acta Neuropathol.* **138**, 103–121 (2019).
- 1236 55. Genin, E. C. *et al.* Mitochondrial defect in muscle precedes neuromuscular junction  
1237 degeneration and motor neuron death in CHCHD10S59L/+ mouse. *Acta Neuropathol.* **138**,  
1238 123–145 (2019).
- 1239 56. Ashrafian, H. *et al.* A mutation in the mitochondrial fission gene Dnm1l leads to  
1240 cardiomyopathy. *PLoS Genet.* **6**, e1001000 (2010).
- 1241 57. Agnew, T. *et al.* A Wars2 mutant mouse model displays OXPHOS deficiencies and activation  
1242 of tissue-specific stress response pathways. *Cell Rep.* **25**, 3315–3328.e6 (2018).
- 1243 58. Fan, W. *et al.* A mouse model of mitochondrial disease reveals germline selection against  
1244 severe mtDNA mutations. *Science* **319**, 958–962 (2008).
- 1245 59. Vafai, S. B. & Mootha, V. K. Mitochondrial disorders as windows into an ancient organelle.  
1246 *Nature* **491**, 374–383 (2012).
- 1247 60. Molinié, T. *et al.* MDH2 produced OAA is a metabolic switch rewiring the fuelling of respiratory  
1248 chain and TCA cycle. *Biochim. Biophys. Acta Bioenerg.* **1863**, 148532 (2022).
- 1249 61. Benard, G. *et al.* Physiological diversity of mitochondrial oxidative phosphorylation. *Am. J.*  
1250 *Physiol. Cell Physiol.* **291**, C1172–82 (2006).
- 1251 62. Beutner, G., Alanzalon, R. E. & Porter, G. A., Jr. Cyclophilin D regulates the dynamic  
1252 assembly of mitochondrial ATP synthase into synthasomes. *Sci. Rep.* **7**, 14488 (2017).
- 1253 63. Carraro, M. *et al.* The Unique Cysteine of F-ATP Synthase OSCP Subunit Participates in  
1254 Modulation of the Permeability Transition Pore. *Cell Rep.* **32**, 108095 (2020).
- 1255 64. Chinopoulos, C. *et al.* Modulation of F<sub>0</sub>F<sub>1</sub>-ATP synthase activity by cyclophilin D regulates  
1256 matrix adenine nucleotide levels. *FEBS J.* **278**, 1112–1125 (2011).

- 1257 65. Giorgio, V. *et al.* Cyclophilin D modulates mitochondrial F<sub>0</sub>F<sub>1</sub>-ATP synthase by interacting  
1258 with the lateral stalk of the complex. *J. Biol. Chem.* **284**, 33982–33988 (2009).
- 1259 66. Lu, Y.-W. *et al.* Human adenine nucleotide translocases physically and functionally interact  
1260 with respirasomes. *Mol. Biol. Cell* **28**, 1489–1506 (2017).
- 1261 67. Benegiamo, G. *et al.* The genetic background shapes the susceptibility to mitochondrial  
1262 dysfunction and NASH progression. *J. Exp. Med.* **220**, (2023).
- 1263 68. Sterky, F. H., Lee, S., Wibom, R., Olson, L. & Larsson, N.-G. Impaired mitochondrial transport  
1264 and Parkin-independent degeneration of respiratory chain-deficient dopamine neurons in vivo.  
1265 *Proc. Natl. Acad. Sci. U. S. A.* **108**, 12937–12942 (2011).
- 1266 69. Wittig, I., Braun, H.-P. & Schägger, H. Blue native PAGE. *Nat. Protoc.* **1**, 418–428 (2006).
- 1267 70. Gilda, J. E. & Gomes, A. V. Stain-Free total protein staining is a superior loading control to  $\beta$ -  
1268 actin for Western blots. *Anal. Biochem.* **440**, 186–188 (2013).
- 1269 71. Kulak, N. A., Pichler, G., Paron, I., Nagaraj, N. & Mann, M. Minimal, encapsulated proteomic-  
1270 sample processing applied to copy-number estimation in eukaryotic cells. *Nat Methods* **11**,  
1271 319–324 (2014).
- 1272 72. Rappsilber, J., Mann, M. & Ishihama, Y. Protocol for micro-purification, enrichment, pre-  
1273 fractionation and storage of peptides for proteomics using StageTips. *Nat Protoc* **2**, 1896–  
1274 1906 (2007).
- 1275 73. Tyanova, S., Temu, T. & Cox, J. The MaxQuant computational platform for mass  
1276 spectrometry-based shotgun proteomics. *Nat Protoc* **11**, 2301–2319 (2016).
- 1277 74. Schwanhäusser, B. *et al.* Global quantification of mammalian gene expression control. *Nature*  
1278 **473**, 337–342 (2011).
- 1279 75. Tyanova, S. *et al.* The Perseus computational platform for comprehensive analysis of  
1280 (prote)omics data. *Nat. Methods* **13**, 731–740 (2016).
- 1281 76. Perez-Riverol, Y. *et al.* The PRIDE database and related tools and resources in 2019:  
1282 improving support for quantification data. *Nucleic Acids Research* **47**, D442–D450 (2019).
- 1283 77. Vizcaíno, J. A. *et al.* ProteomeXchange provides globally coordinated proteomics data  
1284 submission and dissemination. *Nat Biotechnol* **32**, 223–226 (2014).

- 1285 78. Köster, J. & Rahmann, S. Snakemake--a scalable bioinformatics workflow engine.  
1286 *Bioinformatics* **28**, 2520–2522 (2012).
- 1287 79. Dobin, A. *et al.* STAR: ultrafast universal RNA-seq aligner. *Bioinformatics* **29**, 15–21 (2013).
- 1288 80. Liao, Y., Smyth, G. K. & Shi, W. featureCounts: an efficient general purpose program for  
1289 assigning sequence reads to genomic features. *Bioinformatics* **30**, 923–930 (2014).
- 1290 81. Ewels, P., Magnusson, M., Lundin, S. & Käller, M. MultiQC: summarize analysis results for  
1291 multiple tools and samples in a single report. *Bioinformatics* **32**, 3047–3048 (2016).
- 1292 82. Love, M. I., Huber, W. & Anders, S. Moderated estimation of fold change and dispersion for  
1293 RNA-seq data with DESeq2. *Genome Biol.* **15**, 550 (2014).
- 1294 83. Livak, K. J. & Schmittgen, T. D. Analysis of Relative Gene Expression Data Using Real-Time  
1295 Quantitative PCR and the  $2^{-\Delta\Delta CT}$  Method. *Methods* **25**, 402–408 (2001).
- 1296 84. Severgnini, M. *et al.* A rapid two-step method for isolation of functional primary mouse  
1297 hepatocytes: cell characterization and asialoglycoprotein receptor based assay development.  
1298 *Cytotechnology* **64**, 187–195 (2012).
- 1299 85. Pantano, L. *et al.* Molecular characterization and cell type composition deconvolution of  
1300 fibrosis in NAFLD. *Sci. Rep.* **11**, 18045 (2021).

1301

## 1302 **Acknowledgments**

1303 We thank David Hardy and Maryse Moya-Nilges for the histology services, Priscilla Lopes and for  
1304 technical assistance. We thank Nils-Göran Larsson for providing mitoYFP mice, Arnaud Mourier  
1305 and Marie Lagouge for inciteful discussions, and Marie Lemesle for excellent administrative  
1306 assistance. T.W. is supported by the European Research Council (ERC) Starting Grant No.  
1307 714472 (Acronym “*Mitomorphosis*”) and the Agence Nationale pour la Recherche (ANR-20-CE14-  
1308 0039-02). D.A.S and D.H.H are supported by grants from the Australian National Health and  
1309 Medical Research Council (GNT2009732) and Medical Research Future Fund (MRF2016030). We  
1310 acknowledge the Bio21 Mass Spectrometry and Proteomics Facility (MMSPF) for the provision of  
1311 instrumentation, training, and technical support.

# Figure 1

bioRxiv preprint doi: <https://doi.org/10.1101/2023.04.26.538374>; this version posted April 28, 2023. The copyright holder for this preprint (which was not certified by peer review) is the author/funder, who has granted bioRxiv a license to display the preprint in perpetuity. It is made available under aCC-BY 4.0 International license.

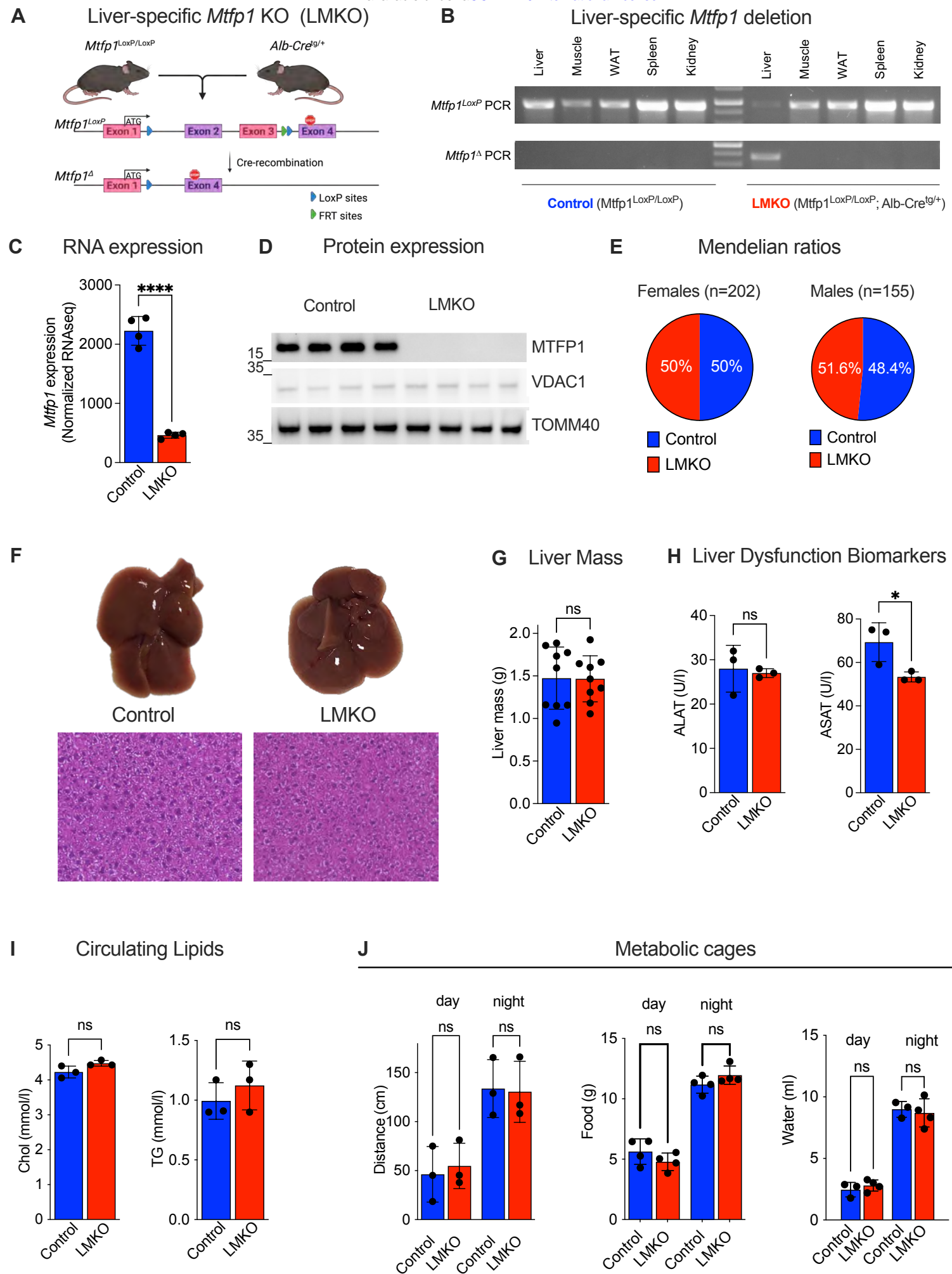
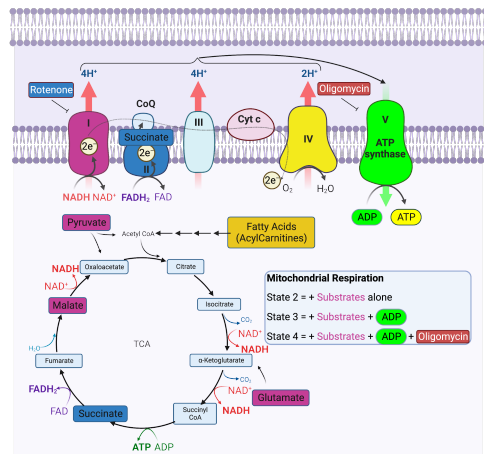


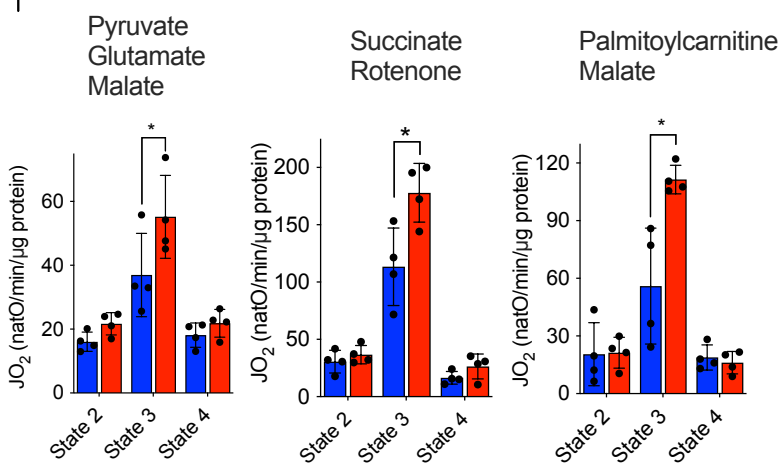


**Figure 2** Oxygen Consumption

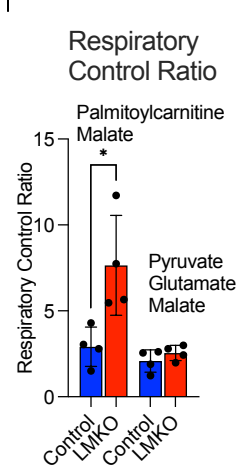
**A**



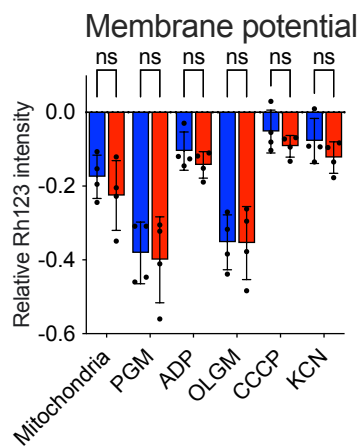
**B**



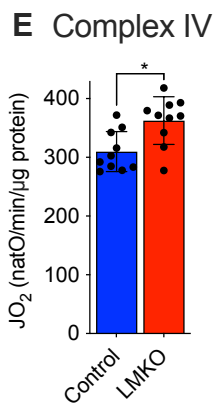
**C**



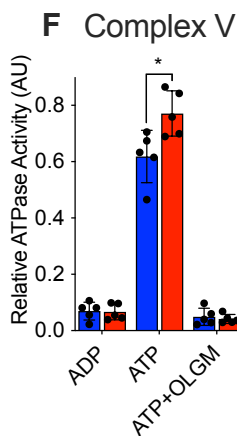
**D**



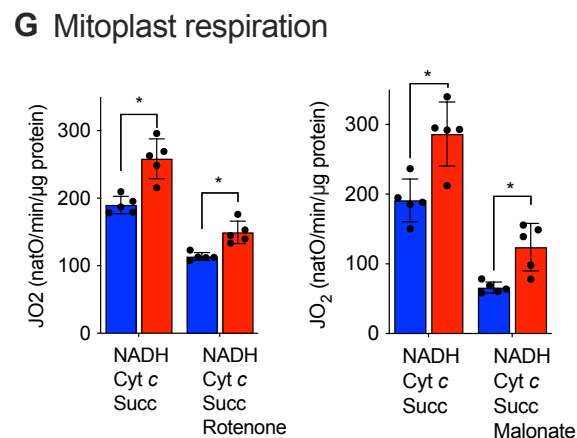
**E**



**F**

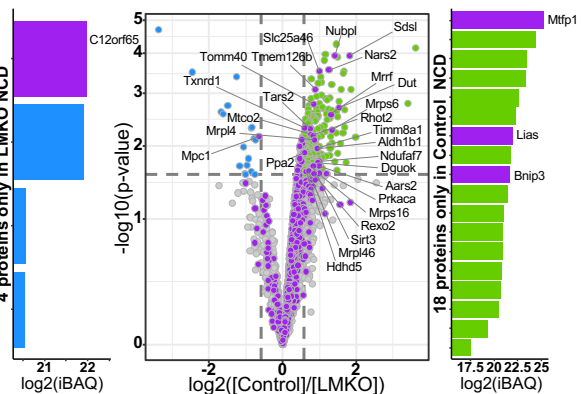


**G**

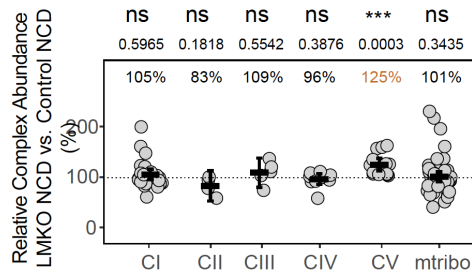


**H**

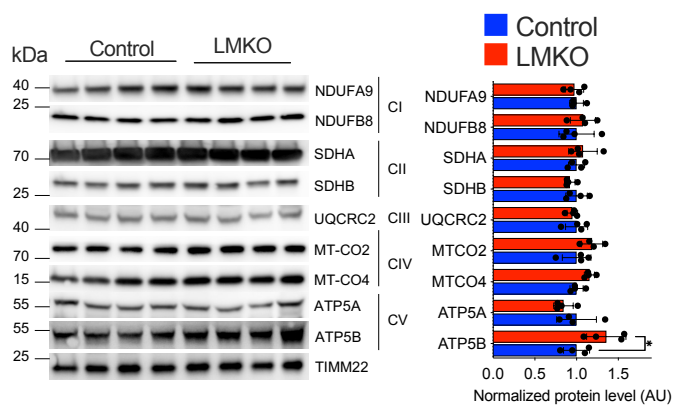
Liver proteome



Relative Complex Abundance



**I**



**J**

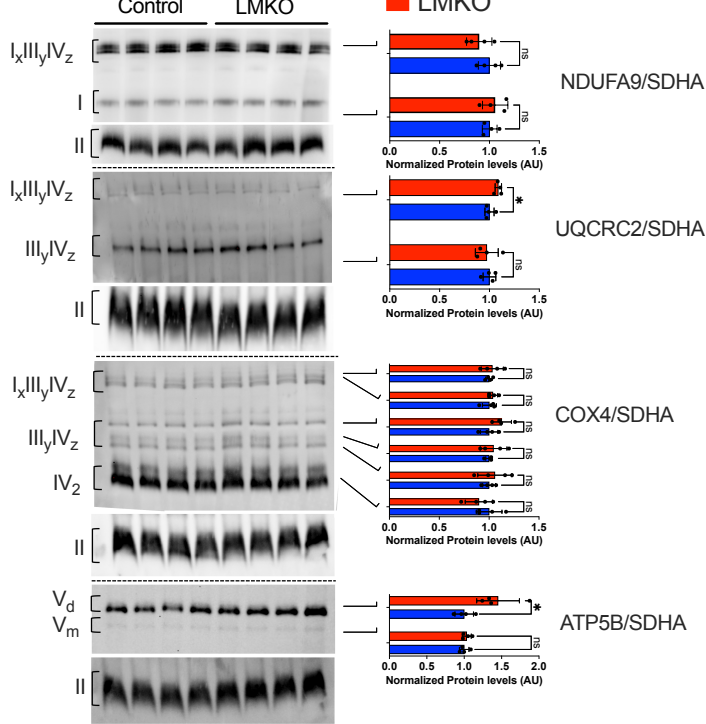


**Figure 3**

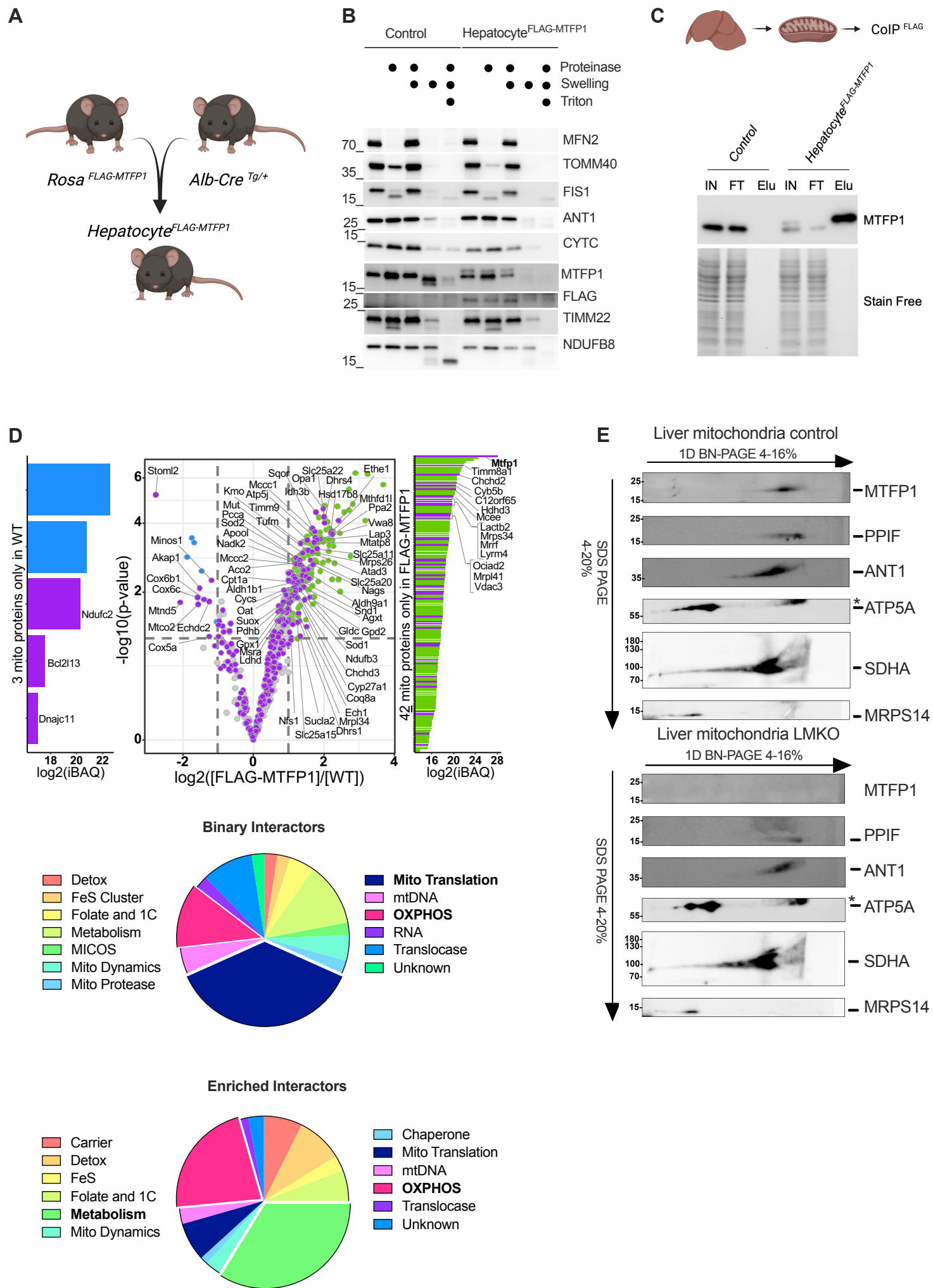


**Figure 4**

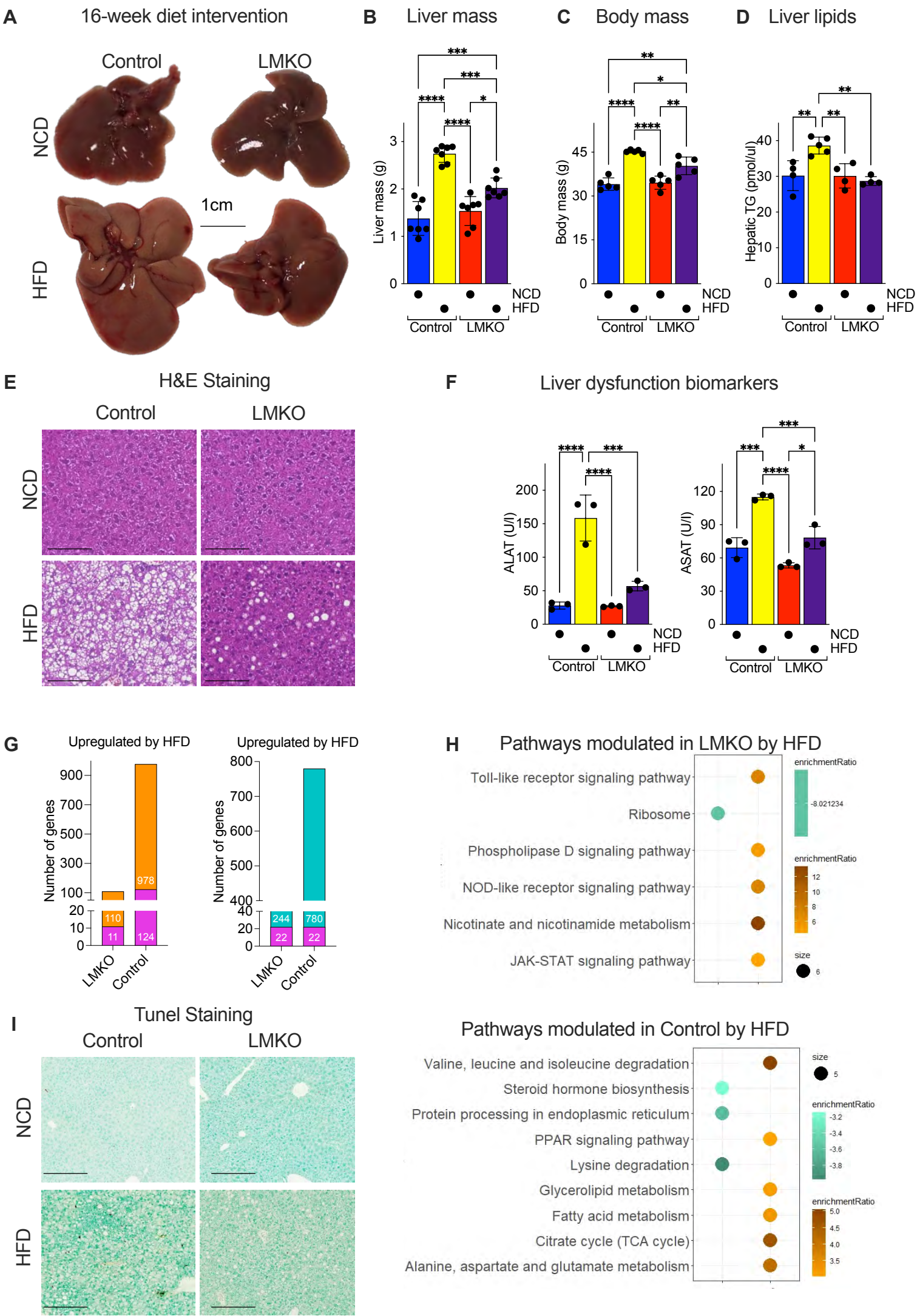


**Figure 5**

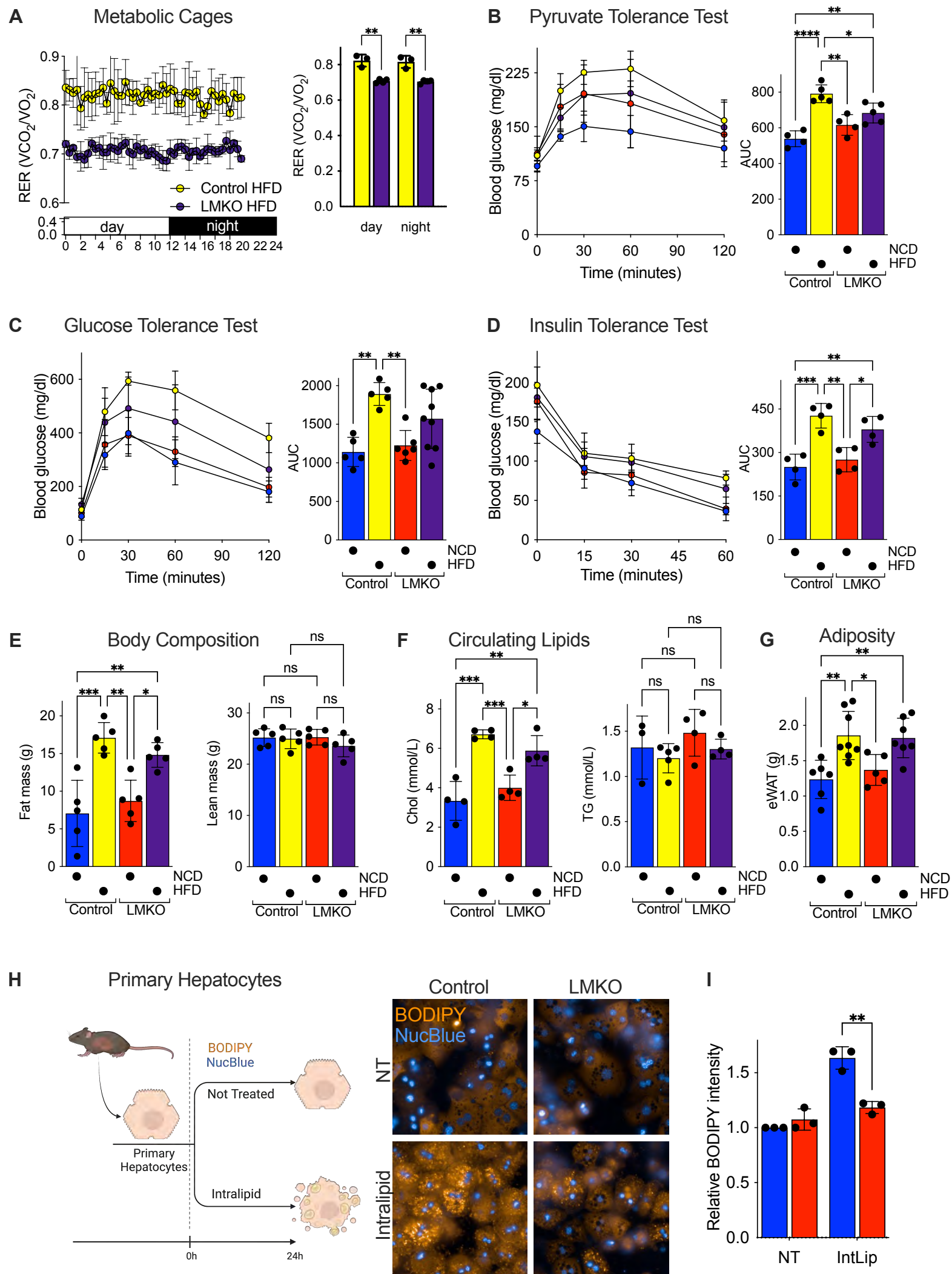


**Figure 6**

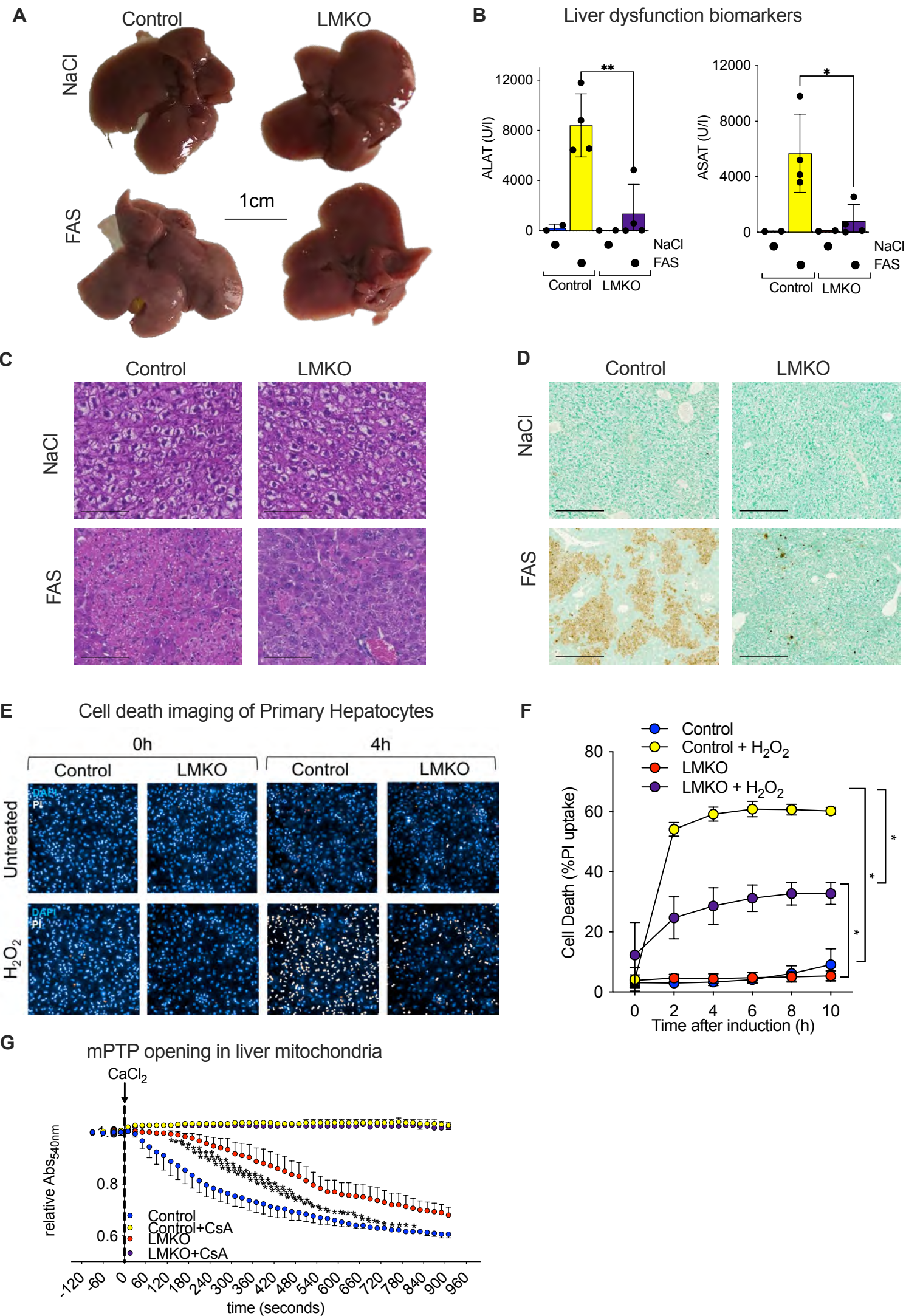


Figure 7

